May 2016

Applied hyperspectral LIDAR for monitoring fauna dispersal in aquatic environments

Klas Rydhmer, Alfred Strand

Division of Combustion Physics
Lund University

Master of Science Thesis

May 2016

Lund Reports on Combustion Physics, LRCP-196
ISNR LUTFD2/TFC-196-SE
ISSN 1102-8718

Klas Rydhmer, Alfred Strand
Department of Combustion Physics
Department of Physics
Faculty of Engineering LTH
Lund University
P.O. Box 118
S-221 00 Lund
Sweden

Abstract

This thesis work has been focused on evaluation and further development of a hyperspectral LIDAR (Light Detection And Ranging) system made by Ljungholm et. al. [1] for monitoring of aquatic fauna, and in particular zooplankton. The project, which was a "proof-of-concept", showed the possibility to create a relatively compact and low-cost LIDAR with both spectral, temporal and range resolution. Experiments were developed with the help of the Department of Limnology, Lund University and performed with the LIDAR system. The dispersal rate of the zooplankton genus *Daphnia* in a water tank was measured, and was found to be largely dependent on background light and laser duty cycle of the LIDAR. The intrusive degree of the laser was determined to be large, since the zooplankton genus *Daphnia* was attracted to the laser light source, but reduced by employing a low duty cycle. The laser intensity stabilisation was ensured by a ramp time before each duty cycle.

Range resolution measurements showed that the modelled resolution was not achieved, and this was determined to be due to defocusing and misalignment of the LIDAR system. The defocusing problem also lead to a weakening of the signal by approximately a factor 10^2, and artifacts were introduced on the detector.

Measurements on the interaction kinetics between the *Daphnia* and the midge larvae *Chaoborus* were performed, and species distinction was made by labelling the different species with different dyes and recording the wavelength spectrum. No interaction statistics could be deduced from the results, mainly due to the inactivity of *Chaoborus*. However, the dyeing of the aquatic fauna using marker pens were shown to be an easy way to label different species for spectral distinction.

Lastly, 3D-scanning of a terrestrial plant was performed, with the aid of a simple robot acting as a whiskbroom LIDAR. The results were promising and the chlorophyll was readily distinguished from the branch, although the range resolution and uneven movement of the robot resulted in a relatively low image resolution.

Acknowledgements

We would like to express our gratitude to the following people for their contribution to this project:

To Mikkel, who made it possible for us to perform this project, and who has supervised us through the entire process. For all his help, discussion and advice, it has been indispensable.

To Elin, who has co-supervised us and given us a lot of helpful advice and encouragement along the way, and for building the Johnson counter.

To Guangyu, for a major help in the experimental work, contributions of figures, and many well needed anecdotes and laughs.

To Joakim, for helpful discussions and advice.

To Lars-Anders and Guiseppe, for help in defining the aquatic experiments and providing *Daphnia*.

To Igor, for building the laser control box.

To Samuel for advice and discussions.

To Maja for her excellent work as lab assistant.

We would also like to thank all *Daphnia* for a great cooperation. We do however kindly refuse further work with *Chaoborus* since they developed wings and flew away during the final weeks of our work. (They also smelled bad.)

Contents

1 Introduction

1.1 Background

1.1.1 Motivation for plankton monitoring

Plankton refers to any small biota living in water which are mainly transported with the aid of currents. Sizes of individual plankton ranges from micrometers to centimeters. Phytoplankton, also known as plant plankton, converts energy from sunlight to chemical energy through photosynthesis and this nutrition is transferred up the food chain through zooplankton to fish and other larger aquatic animals [2]. Phytoplankton are also responsible for fixation of CO_2, and more than 50% of the primary production carbon may cycle through plankton [3]. Figure 1.1 shows two examples of zooplankton, *Daphnia Magna* and *Copepod Calanus*.

(a) *Daphnia Magna. Image from [4]*

(b) *Copepod Calanus. Image from [5]*

Figure 1.1: *Zooplankton.*

The monitoring of plankton is of interest when the status of an aquatic ecosystem is to be analysed or investigated. Both phytoplankton and zooplankton are key components in the food chain, and there is a direct link between fish and plankton populations, since plankton is the major source of nutrition for fish [6]. Because of their close link to fish abundance, plankton populations have important economic consequences for fishery industries [7].

Plankton is a good indicator of water quality and climate change. They respond very fast to changing conditions such as light, temperature and nutrient availability. Changes in climate can affect the timing of the plankton blooms, and the effects pass on up the food chain. Longer term climate change can change the plankton species composition, which may lead to major disturbances in the ecosystem [8]. Furthermore, plankton are highly susceptible to acidification, overfishing and anthropogenic pollution, and the health and condition of the plankton can give information about eutrophication [2] [9] [10]. Therefore, information such as plankton dispersal, concentration, size distribution and species composition is very important in order to gain further knowledge about how aquatic ecosystems behave and change.

1.1.2 Existing methods for zooplankton monitoring

The traditional way of monitoring zooplankton is sampling by use of nets, pumps or other point sampling methods, followed by microscope analysis. These methods are still needed for determination of species composition, size distributions and other detailed properties, but they are cumbersome, time consuming, have low sampling frequencies and coarse spatial resolution. It is also hard to choose which species to measure on since certain net mesh size will collect individuals larger than this size from any species. Because of the limits of these methods, both acoustic and optical monitoring systems have been employed for plankton monitoring, and some of these techniques are described below.

When monitoring phytoplankton concentration over large areas, a wide variety of remote sensing methods are employed. Satellite data is used for monitoring environmental parameters such as concentration of chlorophyll and different pollutions in oceans and lakes. Airborne LIDAR systems are employed for the same applications, but also to detect schools of fish and zooplankton [11] [12].

The NOAA (National Oceanographic and Atmospheric Administration) time-of-flight LIDAR has been used to measure on layers of plankton and to estimate the concentration of zooplankton, but it is incapable of distinguishing between different species of zooplankton. It utilises only the elastic backscattered light to determine the average biomass. The LIDAR has a maximum penetration depth of 24 m, and a depth resolution of 11 cm. [7]

The Zooplankton Acoustic Profiler (ZAP) [13], is an inverted echo sounder, and it consists of an acoustic transducer transmitting at 200 kHz. The ZAP can detect ranges of up to 200 m and it has a range resolution of approximately 12 cm. It operates on the bottom of a water body and gives a vertical profile of the average biomass from bottom to surface. Figure 1.2 presents an image of the ZAP and an example of its measurement data, where the diel vertical migration of zooplankton have been studied (described in section 2.1.2).

(a) *Image of the Zooplankton Acoustic Profiler (ZAP) by Lemon et. al. [13].*

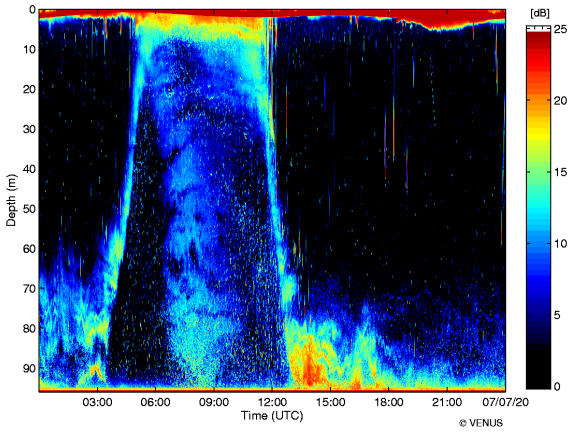

(b) *Data from ZAP, showing the diel vertical migration of zooplankton. Image from [14].*

Figure 1.2: *Zooplankton Acoustic Profiler (ZAP).*

The BIO-MAPER II, is an underwater monitoring system which combines acoustic and optical sensoring. It uses an Acoustic Backscatter Sonar System (ABSS) and a Video Plankton Recorder (VPR). The ABSS measures the backscattered acoustic energy which is related to zooplankton

biomass, and consists of 10 acoustic transducers, 5 pointing upwards and 5 pointing downwards, allowing it to map a larger portion of the water column (within the range of the transducers, which is about 250 m). The VPR (described below) provides ground truthing, although only in a very small section of the probe volume [15] [16]. A schematic of the BIO-MAPER II along with sample data is shown in figure 1.3.

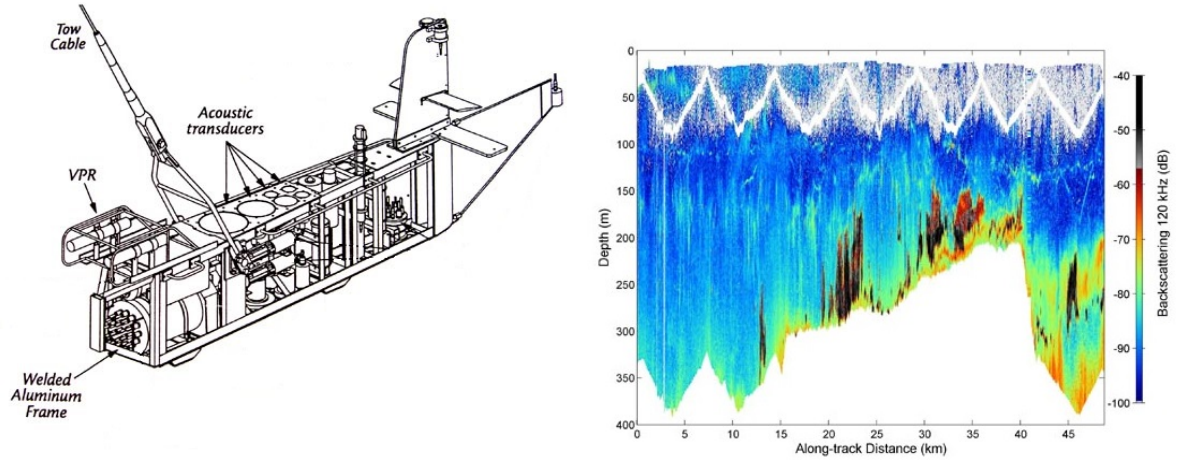

(a) *Schematic figure of the BIO-MAPER II by Wiebe et. al. [16].*

(b) *Sample data from the BIO-MAPER II. Image from [17].*

Figure 1.3: *BIO-MAPER II.*

An advantage of acoustic methods is that sound waves are not attenuated in the same degree as light, thus enabling detection at further ranges. However, acoustic monitoring systems do not have good enough resolution (1 cm at best) to be able to resolve details of zooplankton, unless information about the shape and acoustic response is known beforehand. This limitation means that acoustic methods alone cannot be used to extract information about taxonomy, size and shape of plankton. [18]

Submersible vehicles equipped with different video recorders have been used for *in-situ* monitoring of zooplankton. The Video Plankton Recorder (VPR) developed by Davis et. al. [19] consists of a camera unit and a strobe light aimed toward each other. The strobe light acts as a camera flash and illuminates plankton which are in the field of view of the camera. It is capable of collecting data automatically and continuously, and can provide taxonomic analysis of the data in near-real time. A problem with this technique is its degree of intrusiveness, since the distance between the strobe and camera is 1 m, inducing turbulence in the field of view. The probe volumes are also very small (between 1 ml-1 l) which means that it is unsuitable for probing large areas. A schematic of the VPR is presented in figure 1.4a.

Digital in-line holography is used to monitor zooplankton behaviour, especially swimming trajectories, but can also be used for taxonomic evaluation. The problem of focusing on small and sparsely distributed zooplankton is solved by post-focusing, where the wavefront at the target is reconstructed from the diffraction pattern (i.e. the hologram detected on the CCD). Katz et. al. [18] have developed a submersible in-line holography system to be able to classify individual zooplankton *in-situ*, and to see how they move in time. The advantage of holography over ordinary video recording, as used in the VPR, is the ability to resolve a much larger probe volume due to the wider depth of focus. Figure 1.4b illustrates a schematic of the setup.

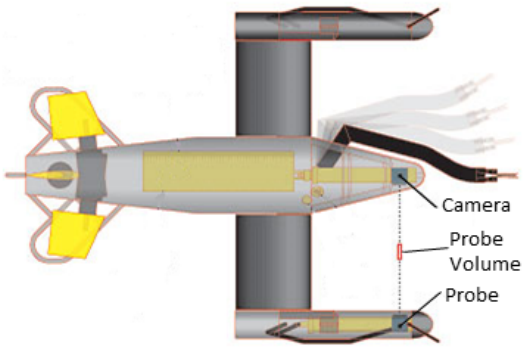

(a) Schematic figure of the Video Plankton Recorder (VPR) submersible system by Davis et. al. [19].

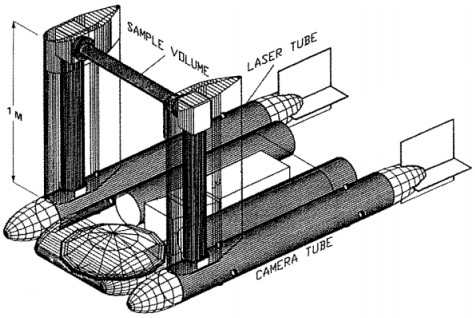

(b) Schematic figure of the in-line holography submersible system by Katz et. al. [18].

Figure 1.4: *Examples of existing zooplankton monitoring systems.*

The LIDAR system developed by Ljungholm et. al. [1] used in this study has the advantage of simultaneously achieving both spectral, temporal and range resolution. This LIDAR system is hyperspectral and is thus capable of detecting the elastic backscattered light, Raman scattering and fluorescence light. The range resolution is achieved by use of a combination of the Scheimpflug principle and the Hinge rule. It was developed to be used in water, with the aim of monitoring aquatic fauna, specifically zooplankton. The original ambition was to be able to distinguish between different species by looking at different attributes in the wavelength spectrum of the backscattered signal, originating from different substances in their bodies which give rise to auto-fluorescence. Potentials were also to measure size distribution by signal extinction, and to detect oscillations from the limbs of zooplankton. [1]

1.2 Outline and aim

The project performed by Ljungholm et. al., which was a "proof-of-concept", showed the possibility to create a relatively compact and low-cost LIDAR with spectral, temporal and range resolution. The aim of this thesis was to further develop the LIDAR system, investigate its characteristics and perform aquatic measurements. Experiments were developed with the help of the Department of Limnology at Lund University. The dispersal rate of *Daphnia* in a water tank was investigated during different experimental conditions with variations in background light and in the laser configuration. Experiments monitoring the interaction kinetics between *Daphnia* and the midge larvae *Chaoborus* were performed and the auto-fluorescence from *Daphnia* was investigated.

2 Theory

2.1 Aquatic fauna

2.1.1 *Daphnia*

The genus primary used in this study was *Daphnia*, which are planktonic crustaceans and includes more than 100 known species of freshwater plankton. Typical body lengths range between 1-5 mm. An illustration of the *Daphnia* anatomy is presented in figure 2.1. It has 5 thoracic limbs (i.e. limbs on the trunk), used for filtering food and for respiration. The antennae are used for swimming, which it does in a jumping-like behaviour by a beating movement (hence the name *Daphnia*, meaning waterflea). The rapid downward beating of the antennae results in a quick movement upwards, and the relatively high density of the body creates a subsequent sinking. The heart is situated in the back along with the brood chamber where the eggs are developed [20]. The intestine run through the center of the body and usually contains phytoplankton, which may be one of the causes of auto-fluorescence from Daphnia . The beating frequency of the thoracic limbs for *Daphnia Magna*, a species of the *Daphnia* genus, is between 2-8 Hz, depending on food concentration, time of day, oxygen concentration and toxicity of the water. [21]

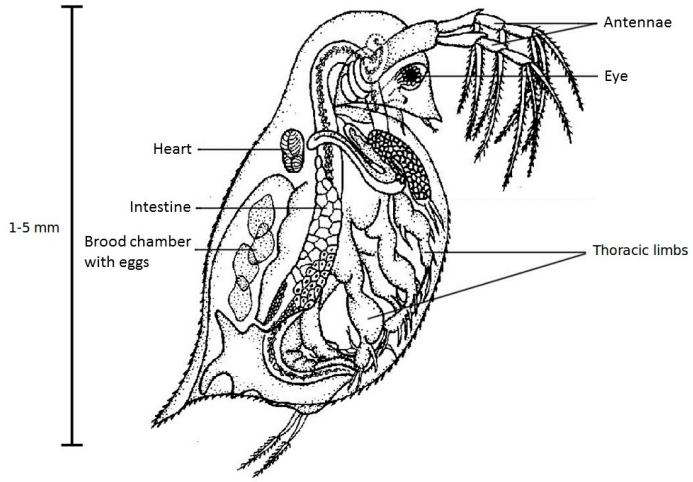

Figure 2.1: *The anatomy of Daphnia. Figure from [22].*

Daphnia feed on small suspended particles, which it filters with the phylopods, flattened leaf-like legs that produce a water current which runs anterior to posterior. The food is usually made up of phytoplankton, and the sizes of the particles consumed are between 1 µm-50 µm. They can be found in a range of water bodies, from large lakes to small pools. Often they are the dominant zooplankton and they therefore play an essential role in the food chain of their aquatic ecosystem. Consequently, *Daphnia* species distribution and life history is closely linked with the occurrence of predators. [20]

2.1.2 Diel vertical migration

A well-known behaviour of zooplankton is the diel vertical migration, where they migrate upwards during nighttime and downwards again during early morning and daytime, as shown in figure 2.2. During daylight, they avoid predators that hunt visually by moving to darker depths, and during nighttime they move to the food rich areas of the illuminated depths. [20]

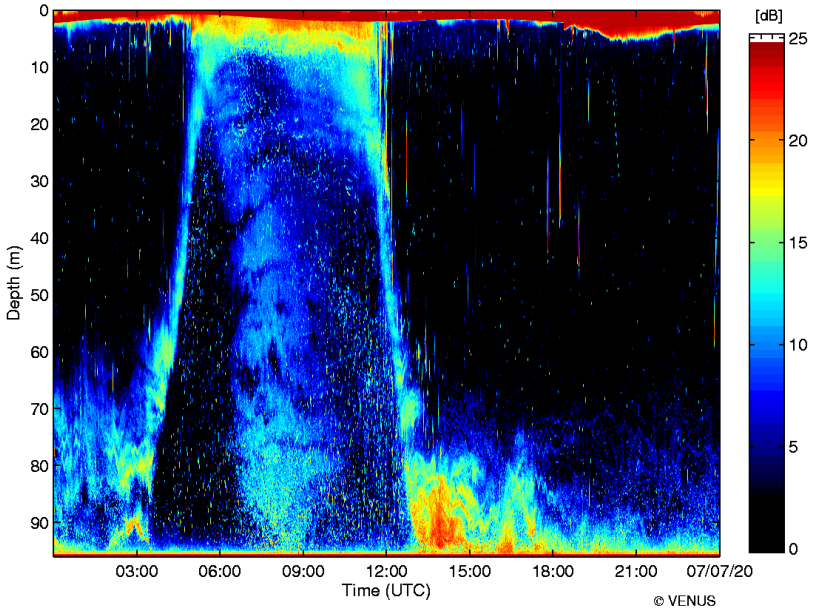

Figure 2.2: *Dial vertical migration, imaged by the ZAP described in section 1.1.2. Between 03:00 and 14:00 the plankton population migrates from a depth of 80 m to the surface and back over a few hours. Image from [14].*

2.1.3 *Chaoborus*

The genus *Chaoborus*, also known as "glassworm", is a type of midge larva, shown in figure 2.3. Its size ranges between 1-2 cm and it has a long, transparent body with two pairs of darkly pigmented air sacks used for vertical migration, and a head with an antenna and a pair of large mandibles [23]. They are opportunistic predators, as they eat different genera of zooplankton. The *Chaoborus* attacks its prey only if it is inside the effective strike area, and does so with a sudden wiggling movement. Since it does not tend to pursue its prey, its interactions with prey is governed by the distribution and swimming behaviour of the prey. Another limiting factor in its feeding is its head and mandible size, which decides how large a prey may be to be digestible by the larva. [24].

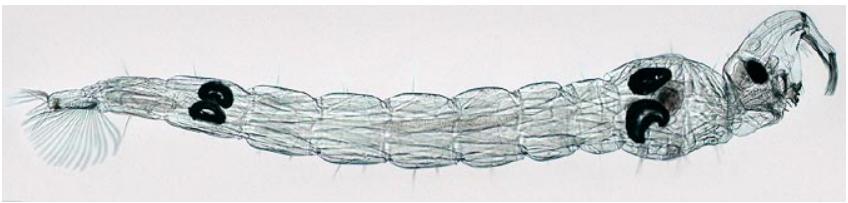

Figure 2.3: *Chaoborus. Image from [25].*

2.2 Light-Matter Interactions

2.2.1 Atomic and Molecular structure

Consider a 2-level atomic system with one electron as shown in figure 2.4 and an energy difference $E = E_2 - E_1$ between the levels. If an incoming photon has an energy which matches the energy difference $E = h\nu$, where h is Planck's constant and ν is the frequency of the photon, then the atomic system may absorb the photon by transitioning to the higher energy level. An atomic system in a excited state may spontaneously decay to the lower energy state by emitting a photon which energy matches the energy difference E, as illustrated in figure 2.4b.

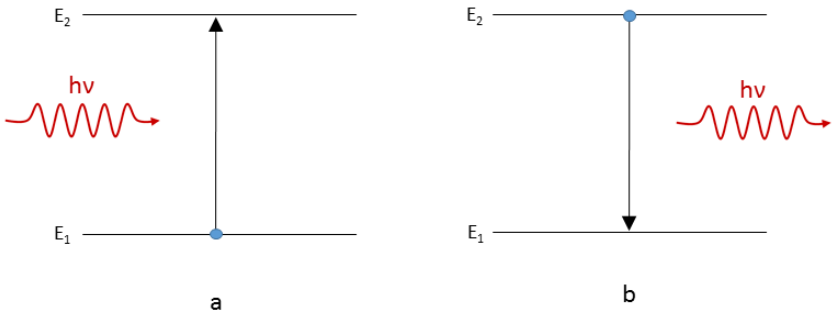

Figure 2.4: *Atoms can change between energy levels by excitation (a) or de-excitation (b) of an electron to a higher or lower electronic state by absorbing or emitting photons, respectively. Absorption and spontaneous emission are two related processes with the same probability.*

The main energy levels in molecules are, as in atoms, the electronic states. The energy difference between two states is usually in the order of a few eV, corresponding to photon wavelengths in the visible or near-IR range. The atoms in a molecule can vibrate and change their positions relative to each other, as illustrated in figure 2.5. These vibrations can occur in many different directions and angles and gives rise to additional energy levels. These vibrational states usually have an energy difference around 0.1 eV, corresponding to far-IR radiation in the electromagnetic spectrum. In addition to vibrations, molecules can also rotate around their center of gravity. These rotations also yields energy levels and these rotational states are generally separated by ca 0.001 eV, which lies in the radio wave region. [26]

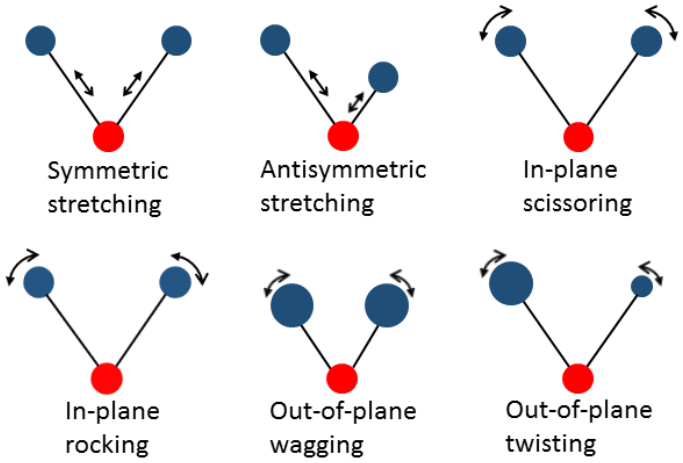

Figure 2.5: *Illustration of the different vibrational modes of a molecule. The OH stretch of water is symmetric (shown in the top left of the figure) and leads to the Raman scattering of water.*

A schematic molecular energy diagram is shown in figure 2.6. For molecules or atoms in gaseous form, it might be possible to distinguish all the separate levels using various spectroscopic methods but for any solid or liquid substance, the energy levels will overlap and form "energy bands" due to the intermolecular interactions [27].

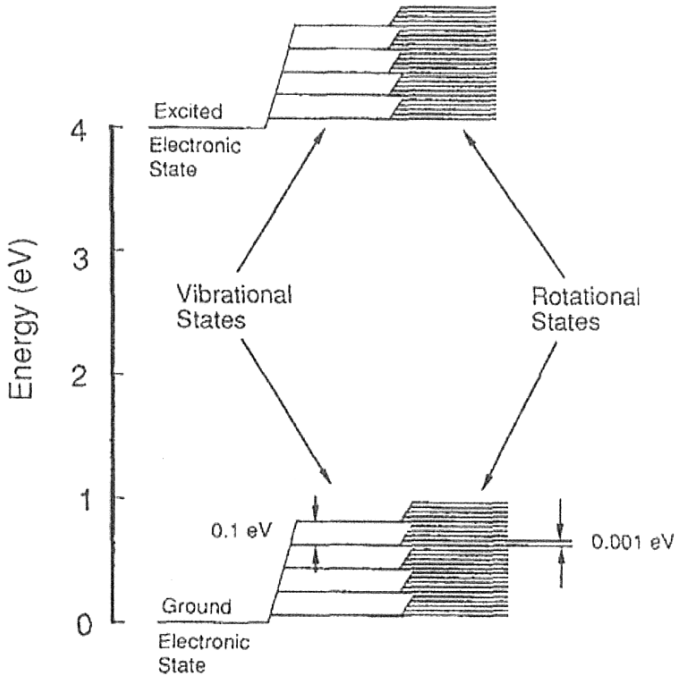

Figure 2.6: *Schematic energy diagram for a molecule. The bounding and relationship between the atoms causes additional energy levels, compared to an atom which only have the electronic states. Figure from [28].*

2.2.2 Fluorescence

Fluorescence is an inelastic process where a molecule absorbs light and then emits light with, in most cases, a longer wavelength. The molecules are excited from a ground state to any vibrational level in a higher electronic state, as illustrated in figure 2.7. By fast (ps timescale) radiation-less processes they are transferred down to the lowest level in the excited state. The fluorescence lifetime is the time in which the molecule remains in the excited state before it de-excites down to a vibrational level in the ground state by emitting a photon. [29]

The emitted photon will have an energy corresponding to the energy difference between the lowest level in the excited state and the vibrational level in the ground state and thus be lower than the exciting photon. Since the transfer down to the lowest level in the excited state is radiationless, the fluorescence spectrum is not directly dependent on the excitation wavelength as long as the excitation energy corresponds to the energy difference between the two electric states [30]. A large number of spectroscopic applications utilises the fluorescent information to characterise the examined object, e.g. in biology where fluorescence from chlorophyll A and B can give information about the composition of substances in vegetation. [31]

Quenched fluorescence is a pressure dependent process, where the transition to a lower energy level occurs because of collisions with other atoms and molecules. Quenching is thus radiation-less, resulting in a lower rate of radiative fluorescence. In water, the fluorescence is quenched by mostly dissolved oxygen, but also other unknown quenchers. This results in a much lower cross section for fluorescence and resonant transitions than scattering processes in the case of this study.

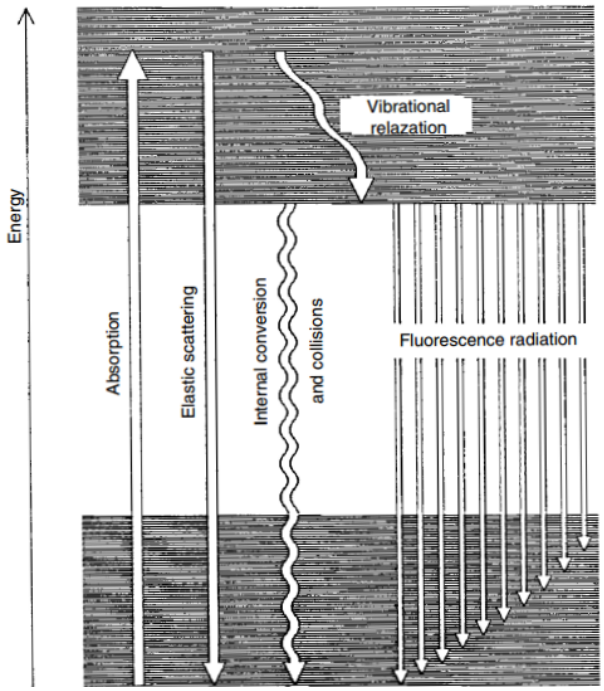

Figure 2.7: *Schematic figure of molecular energy levels. The molecule is excited by a photon to a vibrational level in a higher electronic state. A fast non-radiative relaxation transfers the molecule to the lowest level in the excited state. From there, it can de-excite to any vibrational level in the ground state by emitting a photon with lower energy than the exciting photon. Figure from [30].*

2.2.3 Rayleigh & Raman scattering

Rayleigh scattering is the well known process were light scatters elastically when passing through a medium or colliding with a particle much smaller than the wavelength of the incoming light. The scattering cross section σ is inversely proportional to the wavelength λ; $\sigma = (1/\lambda^4)$ and the scattering occurs when the electromagnetic wave interacts with an atom or molecule of resonant frequency. A molecule present in an electric field $\mathbf{E}$ obtains a dipole moment

$$\mathbf{P} = \alpha\mathbf{E} \tag{1}$$

where α is a polarizability tensor, since the polarization generally is not directed along the electric field. For an oscillating field $\mathbf{E} = \mathbf{E}_0\sin(2\pi\nu t)$, the polarization will vary with the frequency ν and time t, resulting in re-radiation of light of the same frequency.

As discussed earlier, the molecular degrees of freedom includes vibration and rotation, which affects the polarizability. The vibrational movement leads to a varying polarizability, and the rotational movement leads to a varying orientation of the molecule with respect to the field, which also varies the polarizability. Therefore the polarizability tensor α has an additional term depending on the vibrational frequency ν_{vibr} and the rotational frequency ν_{rot} respectively:

$$\alpha = \alpha_0 + \alpha_{1v}\sin(2\pi\nu_{vibr}t), \qquad \alpha_{1v} \ll \alpha_0 \tag{2}$$

$$\alpha = \alpha_0 + \alpha_{1r}\sin(2\pi 2\nu_{rot}t), \qquad \alpha_{1r} \ll \alpha_0 \tag{3}$$

where α_0 is the central polarizability tensor and α_{1v} and α_{1r} are the vibrational and rotational polarizability tensors, respectively. Combining this with equation 1 for an oscillating field gives

$$P_{vibr} = \alpha_0 E_0\sin(2\pi\nu t) + \frac{1}{2}\alpha_{1v}E_0[\cos(2\pi(\nu - \nu_{vibr})t) - \cos(2\pi(\nu + \nu_{vibr})t)] \tag{4}$$

$$P_{rot} = \alpha_0 E_0\sin(2\pi\nu t) + \frac{1}{2}\alpha_{1r}E_0[\cos(2\pi(\nu - 2\nu_{rot})t) - \cos(2\pi(\nu + 2\nu_{rot})t)]. \tag{5}$$

A sideband is thus obtained on both sides of the elastic Rayleigh line, as illustrated in figure 2.8, shifted by the vibrational frequency and twice the rotational frequency respectively. These inelastic effects are called Raman scattering, and their strengths are generally 10^{-3} of the strength of the Rayleigh line. The down- and upshifted lines are called Stokes and Anti-Stokes, respectively. In liquid water, there is no rotational spectrum due to hydrogen bonding between the molecules, and consequently only the vibrational Raman band is present. [28] [32]

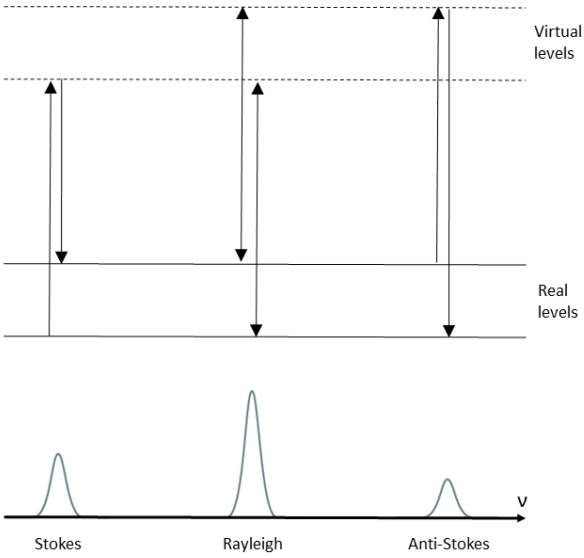

Figure 2.8: *Schematic figure of Rayleigh and Raman scattering. Virtual energy levels are introduced because of the varying polarizability in the molecule. The down- and upshifted Raman lines are called Stokes and Anti-Stokes, respectively.*

The wavelength of the Raman shift is dependent on the wavelength of the excitation photons and can be calculated from energy conservation:

$$E_E - E_{vib} = E_R \tag{6}$$

where E_E is the energy of the excitation photon, E_{vib} the energy of the vibrational level and E_R the energy of the Raman photon. Since $E = hc/\lambda$, where c is the speed of light and λ the wavelength of the photon, the wavelength of the Raman shift is calculated by

$$\frac{1}{\lambda_E} - \tilde{\nu} = \frac{1}{\lambda_R}, \tag{7}$$

where $\tilde{\nu}$ is the wavenumber (E_{vib}/hc) of the vibrational level [33]. In this study, a laser with 445 nm is used and the wavenumber of the vibrational level of the OH-stretch in water is 3350 cm^{-1}, so the Raman scattering wavelength is 523 nm [32].

2.2.4 Mie Scattering

Rayleigh and Raman scattering occurs when the wavelength is much larger than the diameter of the scattering molecules. The process when light is scattered by particles of comparable size to the wavelength or larger is called Mie scattering. Mie theory consists of complete solutions to Maxwell's equations outside and inside of the scattering particle. As the solutions gets very complicated for any irregular shape, a common simplification is to assume a spherical particle for which the solution is analytically possible. [34]

Mie scattering is elastic and the cross section for scattering is largely dependent on particle size, wavelength and the difference in refractive index between the particle and surrounding medium [34]. For particles with sizes much larger than the wavelength, the cross section for scattering is approximately proportional to $1/\lambda^2$. [28]

2.3 Remote sensing

In an environmental context, remote sensing often refers to techniques where electromagnetic radiation is detected from objects or areas such as oceans, forests, land surface or the atmosphere. The properties of the objects can be deduced from both the amount and type of electromagnetic radiation that is backscattered. Often the detectors are mounted on airplanes or satellites, in order to cover large areas. Examples of such applications are time-resolved growth of vegetation, water pollution, erosion and city development. Remote sensing is also used when measuring atmospheric pollutants, usually with a stationary detector. [35]

2.3.1 Time-of-flight LIDAR

The acronym LIDAR stands for Light Detection And Ranging, and is analogous to RADAR, but instead of radio frequencies, other frequencies of the electromagnetic spectrum are used (e.g. visible light, UV and IR). Many different techniques go under the name LIDAR, but the methodology is based on light emission and detection of the backscattered light from the objects of interest. Usually, the light is emitted in the form of laser pulses. When measuring distance, a laser pulse is emitted into the probe volume and the time it takes for the scattered light to reach the detector is measured. The range resolution is $\Delta R = c \cdot \frac{\Delta t}{2}$, where c is the speed of light in the medium and Δt is the pulse duration. A ns-pulse is thus needed to obtain a range resolution of about 1 m. LIDARs are mostly used for ranging, but has many other applications, such as in land surveillance, geodesy, archaeology, terrestrial vegetation monitoring and atmospheric monitoring. [28]

2.3.2 Continuous Wave-LIDAR & the Scheimpflug principle

An alternative method to time-of-flight for achieving range resolution in LIDAR is by employing the Scheimpflug principle, and the setup is illustrated in figure 2.9. The method was invented in 1901 by Carpentier but expanded by Scheimpflug in 1904 [36]. The method is commonly used in photography when different focus distances are wanted at different positions in an image (as in forward facing aerial photography for example).

The lens is angled to shift the focal plane from being parallel to the image plane. This causes objects at different distances in the laser beam, which is placed in the object plane, to be imaged at different positions on the detector. As seen in figure 2.9a, a larger detector covers a larger range interval along the laser beam. The covered area can be moved back and forth along the beam by adjusting the angles ϕ and Θ. For longer ranges, each pixel on the detector will cover a larger distance on the object plane. In a LIDAR setup, the backscattered or fluorescent signal will generally decrease with distance and the larger integration depth can be a positive side effect. This does however not apply for hard targets, since they reflect the same amount of light independent of where they are detected.

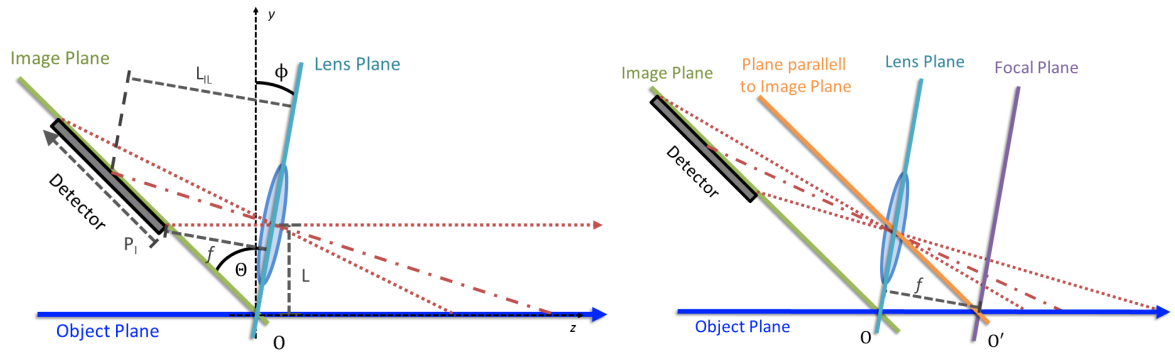

(a) *The Scheimpflug principle.* ***(b)*** *Hinge rule.*

Figure 2.9: *The Scheimpflug criterion is fulfilled when the lens, image and object planes intersects at one point, the Scheimpflug intersect (O). The laser beam is placed in the object plane and the resulting image appear on the image plane. p_I is the pixel position on the detector or slit, z is the distance along the object plane (laser beam), ϕ is the angle of the collecting lens with respect to the object plane, Θ is the angle between the image and lens planes, L is the distance from the center of the lens to the object plane, L_{IL} is the separation distance between the detector or slit and the lens, along the optical axis of the lens. When focusing in the near field, the Hinge intersect (O') between the focal plane and the plane parallel to the image plane through the center of the lens, needs to be positioned on the object plane.*

The relationship between pixel position and corresponding distance in the object plane is given by

$$z = \frac{L[p_I(\sin\Theta - \cos\Theta\tan\phi) + L_{IL}]}{p_I(\cos\Theta + \sin\Theta\tan\phi) + L_{IL}\tan\phi} \tag{8}$$

$$\tan\Theta = \frac{L_{IL}}{L} \tag{9}$$

Where z is the distance along the laser beam, p_I is the position on the detector or slit, L_{IL} is the separation between the center of the lens and center of the slit or detector along the optical axis of the lens, and L is the separation between the center of the lens and the laser beam. ϕ is the angle of the lens with respect to the laser beam and Θ is the angle between the image plane and lens plane [37]. The correct swing angle ϕ for positioning a signal from a given distance z_{ref} on a desired pixel position p_{Iref} can be calculated by

$$\phi = \arctan\frac{L}{z_{ref}} - \arctan\frac{p_{Iref}\cos\Theta(z_{ref} - f)}{z_{ref}f} \tag{10}$$

$$L_{IL} = \frac{z_{ref}f}{z_{ref} - f} - p_{Iref}\sin\Theta \tag{11}$$

Where f is the focal length of the lens [38]. In this study and for aquatic use, an infinite focus is not desired but rather a finite probe volume in the near field. The calibrated pixel - range relation for the setup used in this study is presented in figure 3.9. Since any setup which places the detector and light source according to the Scheimpflug principle and the Hinge rule will be range resolved, it is possible to use a continuous wave (CW) laser as well as a pulsed one.

2.3.3 Comparison between pulsed and continuous LIDAR

A pulsed time-of-flight LIDAR setup is limited in spatial and temporal resolution by the pulse length since the range resolution is $\Delta R = t_p c/2$, where t_p is the length of the laser pulse [28]. The pulse duration and bandwidth are related by the uncertainty principle $t_p = 1/\Delta\nu$, where ν is the frequency of the light, which puts a physical lower limit to the pulse duration if a laser is used as the light source [27]. In a Scheimpflug LIDAR setup, the range resolution is, on the other hand, limited by the pixel size on the detector, the distance between the detector and light source (L in figure 2.9) the field of view (FOV), the point spread function (PSF) and thus the quality of the lenses, allowing a much higher resolution.

The temporal resolution in a pulsed LIDAR setup is also limited by the repetition rate of the laser and the round trip time of the pulse, since the pulses must not overlap. In a CW-LIDAR, the temporal resolution is only limited by the read-out speed of the detector. Table 1 shows a comparison between a pulsed time-of-flight LIDAR and a CW-LIDAR employing the Scheimpflug principle.

	Range resolution	**Signal intensity**	**Transmitter limitation**	**Receiver limitation**	**Sampling limitation**
Time-of-flight LIDAR	Constant	$1/R^2$	Pulse duration	Bandwidth	Sampling rate
Scheimpflug LIDAR	Tangential	Constant	Expander PSF and beam width	Receiver PSF and FOV width	Pixel pitch

Table 1: *Comparison between pulsed and continuous LIDAR. R is the range between target and LIDAR. In this study, the expander is the laser objective, and the receiver is the detector optics. Table created by Guangyu Zhao.*

2.4 Light propagation in water

The attenuation in water is divided into scattering and absorption, and can be described by the Beer-Lambert law, which states that the attenuation A is proportional to the path length and the concentration c of attenuators in the sample:

$$\left.\begin{aligned} A &\equiv \log_{10}\left(\tfrac{I_0}{I_T}\right) = \log_{10}\left(T^{-1}\right) \\ A &= kLc \end{aligned}\right\} \Rightarrow T = e^{-\tilde{k}Lc} \tag{12}$$

where k and $\tilde{k}$ are proportionality constants, L the path length, I_0 and I_T the initial and transmitted intensity, and T the transmittance. [28]

The absorption spectrum of water has been studied in a number of experiments. A sample of the results is found in [39] and table values are plotted in figure 2.10. The absorption is largely determined by the internal energy structure of the molecules were the absorption peaks corresponds to the vibrational levels in the water molecule [40]. The attenuation over a range of 5 m have been calculated using equation 12 and is presented in figure 2.11.

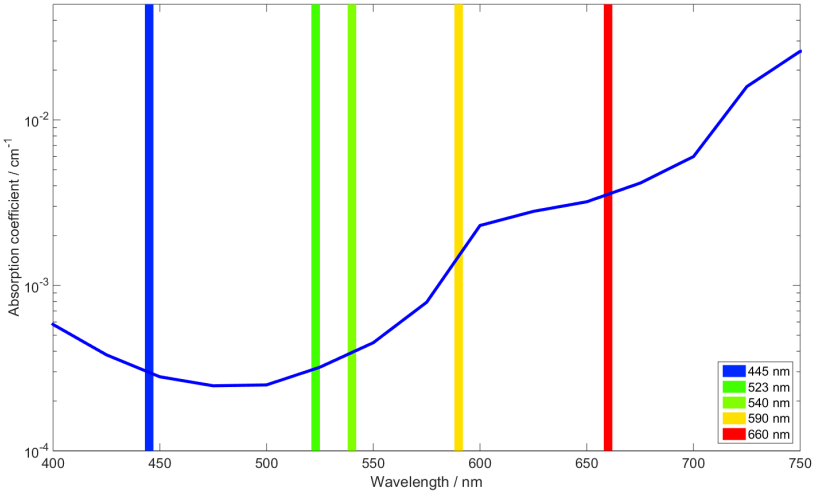

Figure 2.10: *The water absorption spectrum used for calculating the attenuation presented in figure 2.11. Marked wavelengths are: 445 nm (laser), 523 (Raman scattering), 540 nm (fluorescence from green / yellow dye), 590 (fluorescence from orange / pink dye), 660 (Chlorophyll fluorescence). The experimentally measured spectrum is taken from [41].*

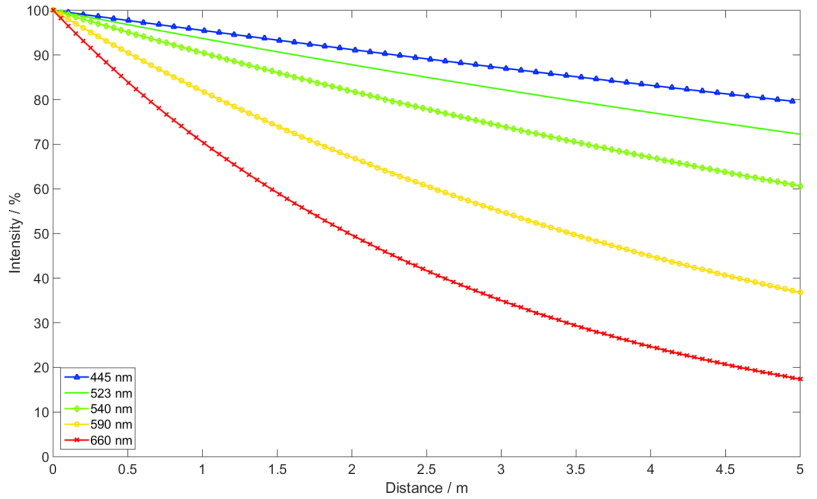

Figure 2.11: *Transmission for used wavelength in pure liquid water. Shown wavelengths are: 445 nm laser, 523 Raman, 540 yellow dye, 590 orange / pink dye, 660 Chlorophyll fluorescence.*

The absorption curve of pure water is approximately temperature independent in the visible region within normal temperature ranges (15 - 30°). The exception is a small peak around 610 nm where the absorption coefficient may vary up to 5% depending on temperature. [42]

3 Instrumental setup & characteristics

3.1 LIDAR system

The LIDAR system used was developed by Ljungholm et. al. [1], and consists of a detector system set up in the Scheimpflug configuration, and a diode laser as the emitter. The detector is a CCD sensor on an ATV Prosilica GC655 camera, which has a 2D-chip with 659x493 pixels and a size of 6.5x4.9 mm. The laser is a 1W GaN laser diode emitting at 445 nm from a chip source with a size of 1x20 µm. The wavelength was chosen because of its low absorption in water and high efficiency for inducing fluorescence in chlorophyll-containing zooplankton. A standard video objective with diameter of 20 mm and focal length of 20 mm is used to expand, collimate and transmit the laser light from the laser chip. The beam shape is Gaussian in the short axis of the laser chip and rectangular/top-hat shaped in the long axis, giving rise to a toothpaste-shaped beam after emission through the objective. The objective has an adjustable focus and an iris for beam shaping. Figure 3.1 shows the complete LIDAR system with laser and detector system (collective lens, slit, spectrometer and camera).

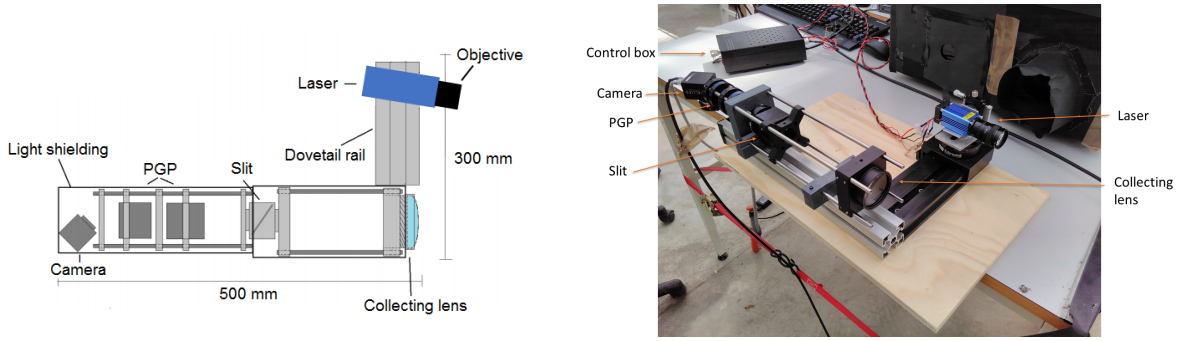

(a) *Schematic figure.* ***(b)*** *Photograph.*

Figure 3.1: *Schematic figure and photograph of the LIDAR system.*

Figures 3.2, 3.3 and 3.4 shows detailed illustrations of the detector system. The collecting lens focuses the light onto the slit which is tilted with respect to the lens so that light from different ranges can be collected (figure 3.3) according to the Scheimpflug principle. The tilt angle of the slit with respect to the collective lens and laser beam determines the range interval that will pass to the detector. The range interval was between 3.4 - 5 m. After passing the slit, the light is collimated by the collimating lens and dispersed by the PGP (Prism-grating-prism) to obtain the wavelength spectrum. The PGP only affects the light in one dimension, thus conserving the range information in the other dimension. Figure 3.3 displays the view from above, which shows that the rays are unaffected by the PGP, and figure 3.4 displays the view from the side, which shows that the PGP disperses the different wavelength on different locations on the detector (CCD chip of the camera). Inside the PGP there is an integrated 450 nm longpass filter to suppress the elastic signal from the laser.

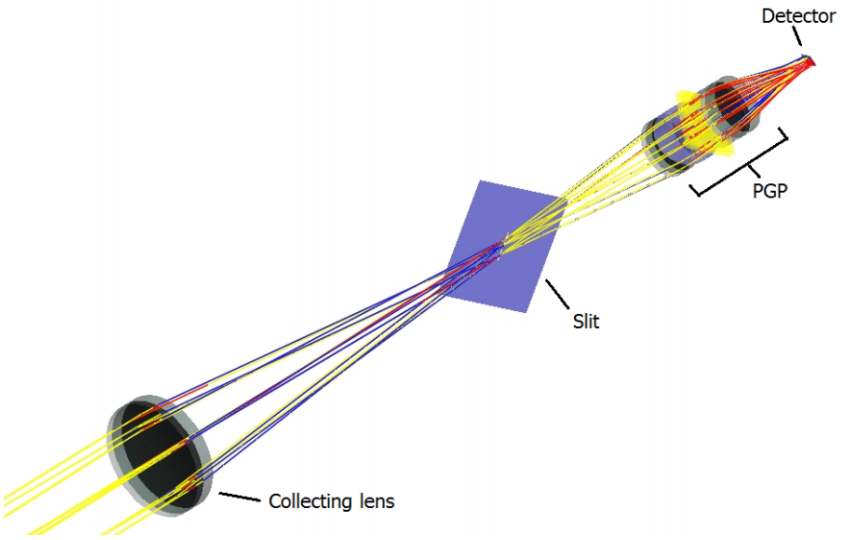

Figure 3.2: *All components of the detector system, viewed from the side. Image made by Ljungholm [1], taken from the modelling software FRED.*

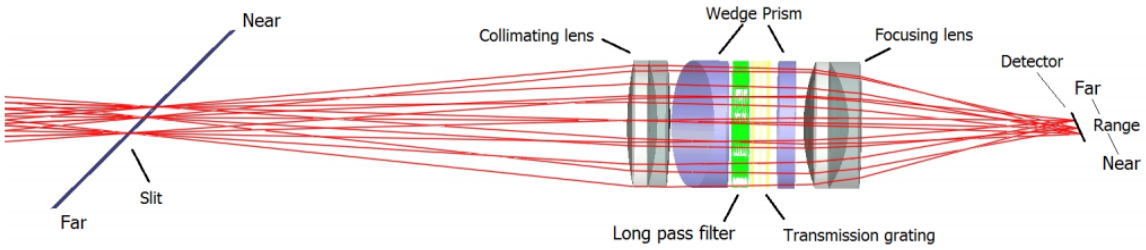

Figure 3.3: *View from above of the detector system. Light from different ranges are directed to different locations on the detector. Image made by Ljungholm [1], taken from the modelling software FRED.*

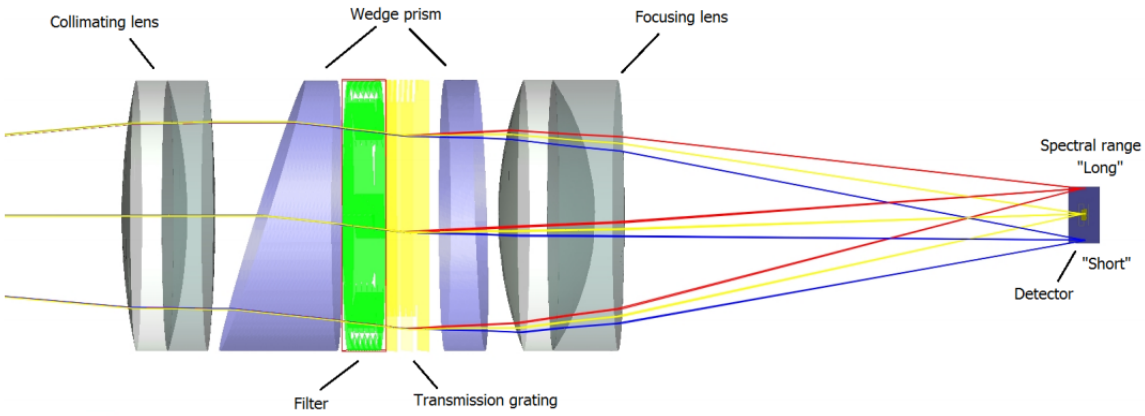

Figure 3.4: *View from the side of the detector system. The PGP disperses the wavelengths so that they are directed to different locations on the detector. Image made by Ljungholm [1], taken from the modelling software FRED.*

3.2 Control system

A LabView control system, developed by Guangyu Zhao was in place at the start of the project. This system was then further developed and improved. Initial problems with read-out speed, uncontrolled saving of data and file labeling were solved and two different versions were developed. The first version is used when the laser is operating in continuous or modulation mode. It allows for control of the exposure time, gain and binning, and displays the recorded data in four windows. The second LabView program allows for periodic measurements, and in addition to the parameters mentioned above, it also allows for configuration of the laser ramp time, number of exposures per duty cycle and the pause time between the cycles. The recorded data are saved continuously and the saved binary files contain information about the detector resolution and a time stamp.

The layout of the interface is shown in figure 3.5. The top left windows shows the signal as it is recorded on the detector, with wavelength on the x-axis and range on the y-axis. The top right window displays the signal intensity as a function of range along three chosen wavelength channels, for example the channels corresponding to the elastic scattering (Rayleigh and Mie), Raman scattering and fluorescence. The bottom left window shows the wavelength spectrum at a given range and the bottom right shows a range-time map for the elastic channel.

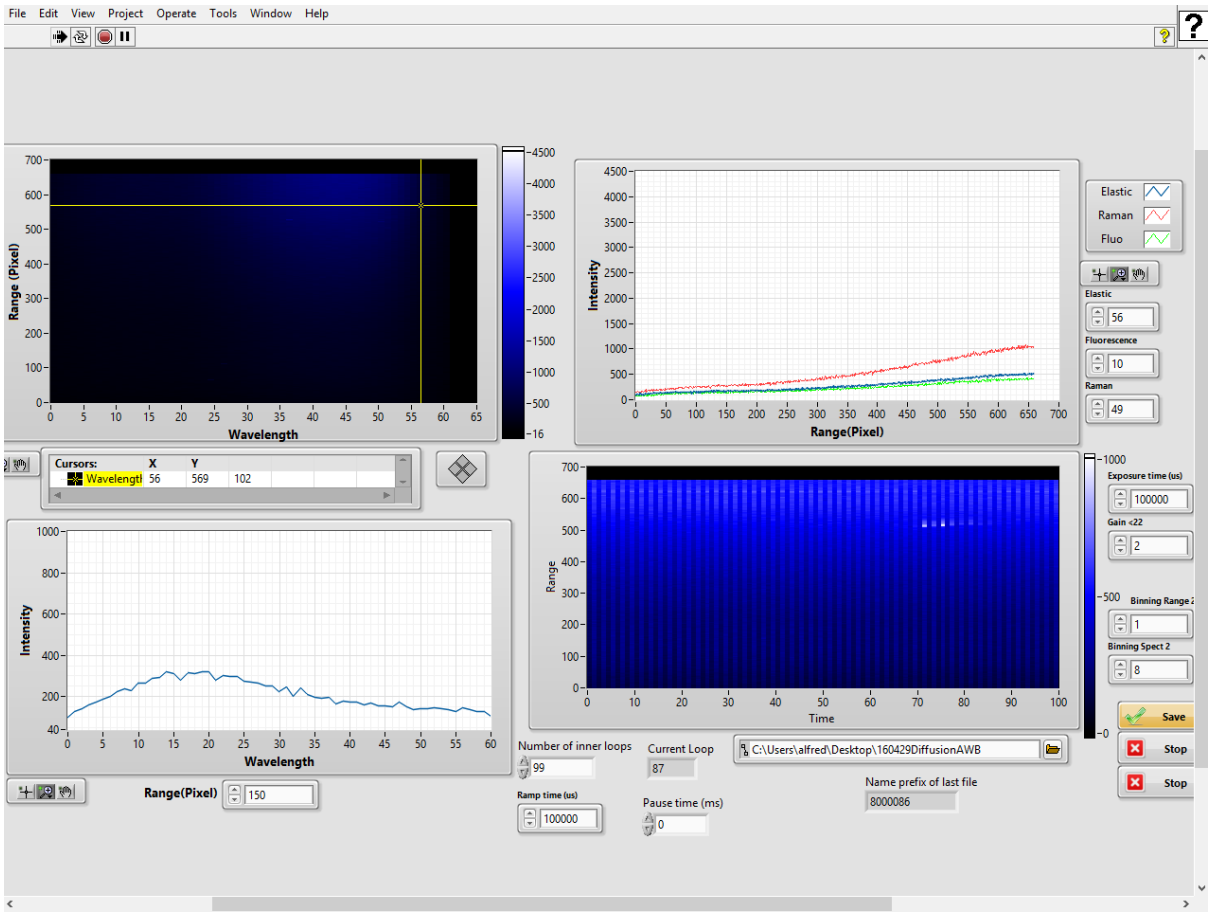

Figure 3.5: *The user interface of the detector. This image is from the periodic program which has a few additional configurations in the lower part of the screen.*

A physical control box, constructed by Igor Buzuk, replaced the current generator used initially. The control box is shown in figure 3.6. The laser is started by turning the key and flipping the "start" switch. This also turns on the red check light on the control box. The laser can then be switched off by turning the key or pressing the "Stop" button. Pressing the stop button will however trigger a fuse which makes a restart impossible and it should only be used as a emergency stop. The flip switch (Ext.trig/Cont.) changes between continuous and modulation mode. In modulation mode, a strobe signal from the camera runs through a Johnson counter inside the control box, which sends out a new strobe every second exposure. This secondary strobe signal is then used to control the laser. The state of the laser can be changed by pushing the button above the flip switch (C.Reset).

Figure 3.6: *The physical control box for the laser, constructed by Igor Buzuk.*

3.3 Calibration

3.3.1 Wavelength

The wavelengths (and light sources) used in the calibration were 445 nm (the blue laser used in the LIDAR system), 532 nm (green laser pointer) and 652 nm (red laser pointer). Initially, an integrating sphere was used which caused very broad spectral lines since the detector is optimised for a point light source on the optical axis. The calibration was therefore remade using black and white paper placed in the optical axis. The lasers were then aimed at the papers and the backscattered light was recorded. A spectrum was recorded to determine the wavelength of the peaks for the three lasers, shown in figure 3.7. The full width at half maximum (FWHM) for the blue, green and red peaks are 15, 10 and 15 nm, respectively.

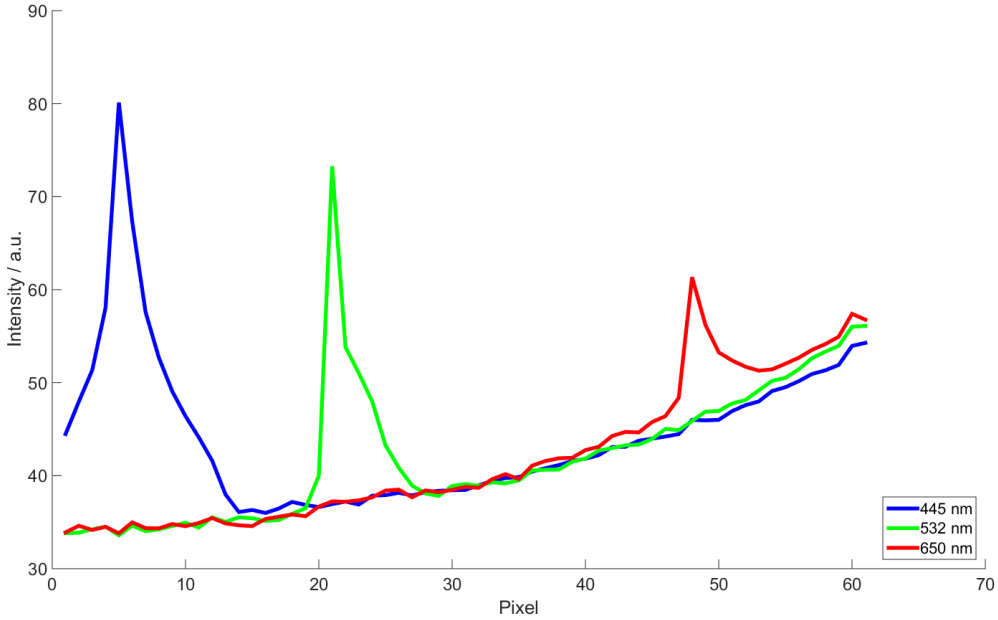

Figure 3.7: *The peaks of the three lasers used in the calibration.*

A first degree polynomial was fit to the data, shown in figure 3.8. This fitted curve was then used in all following results. During experimental work, small adjustments of the angle between the laser and detector (ϕ in figure 2.9) often had to be made to optimise the signal. These changes usually moved the position of the elastic signal on the detector, slightly changing the pixel channel for the elastic signal. These changes are accounted for during the data processing by adjusting the height of the fitted curve in such a way that the elastic channel always corresponds to 445 nm. The wavelength range is approximately 420-720 nm, and with 61 wavelength channels (493 pixels binned by 8), one channel corresponds to 4.9 nm.

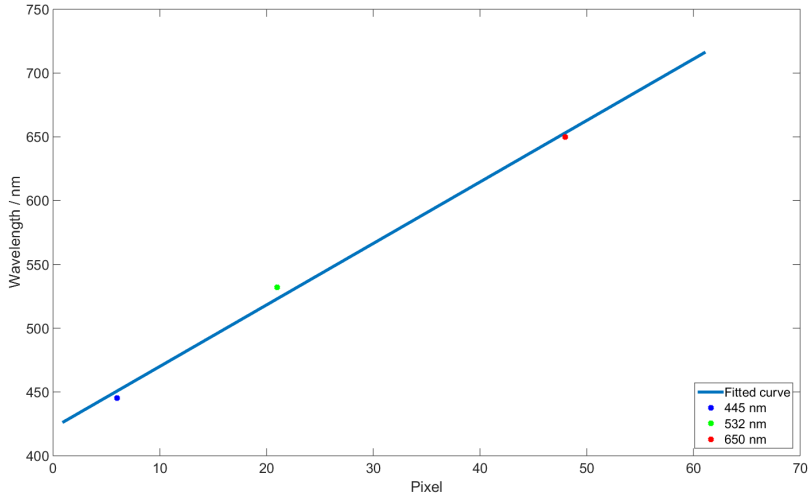

Figure 3.8: *The first degree polynomial fit for the calibration, with the three data points marked as dots with corresponding colour.*

3.3.2 Range

The range curve is calculated by equation 8 for given angles and distances and the result is presented in figure 3.9. The range resolution calibration was performed using a ruler and two strings, approximately 0.2 mm in diameter. Weights were attached to the bottom of the strings which were inserted into the beam with a known separation. The initial separation between the strings was decreased with 2 cm increments to 10 cm and then with 1 cm increments down to 1 cm.

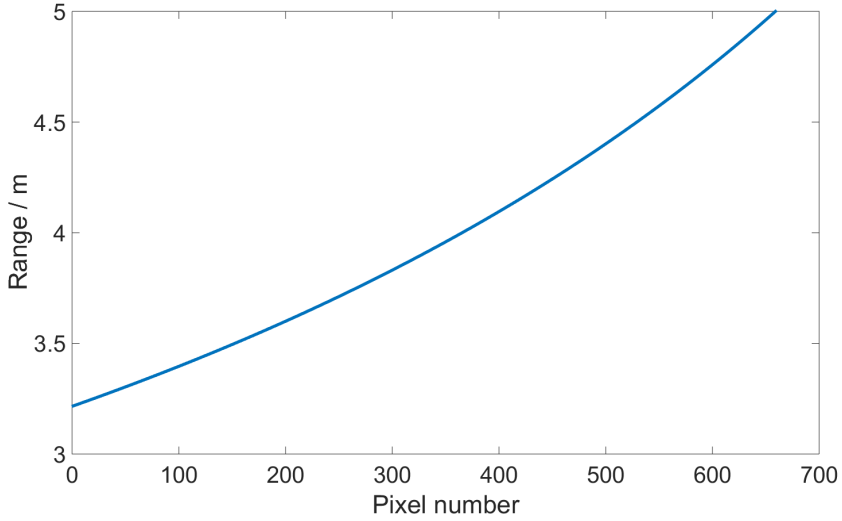

Figure 3.9: *The calculated pixel - range relation for the setup. Due to the trigonometrical arrangement of the optics, the range resolution decreases with distance. The theoretical maximum range resolution varies between 0.17 cm and 0.43 cm along the beam but is in reality limited by the thickness of the laser beam.*

The result from the range calibration is shown in figures 3.10, 3.11 and 3.12 where the different colours represent different string separations. In the near end of the tank, two individual peaks can be resolved with a separation of 5 cm. In the center of the tank, this distance is reduced to 7 cm and in the far end, the minimum distance is around 9 cm. The reduction in resolution with distance follows from the Schemipflug principle as discussed in section 2.3.2.

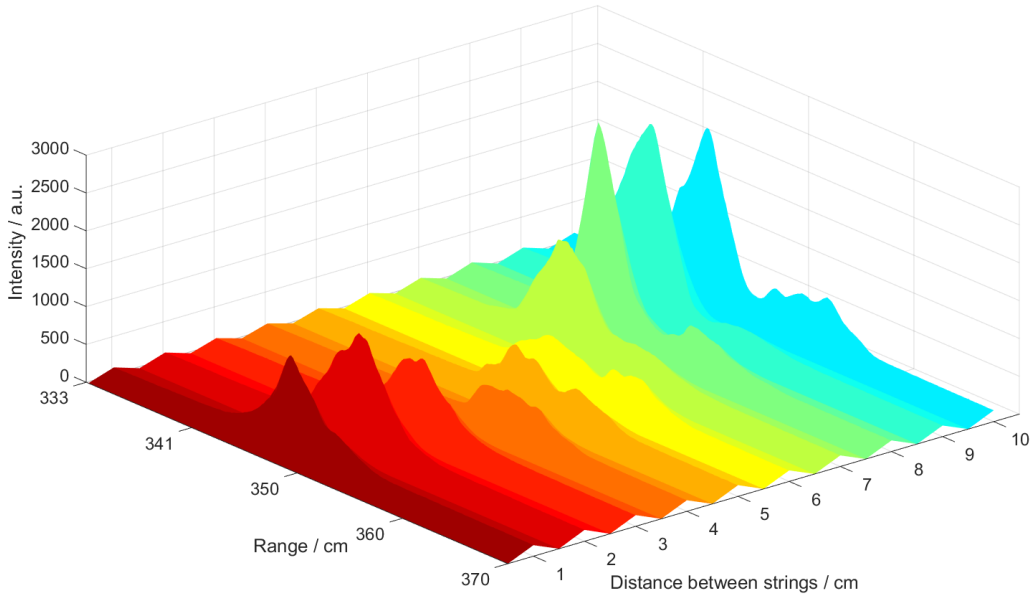

Figure 3.10: *Range resolution in the close end of the probe volume. Different colors correspond to different distances.*

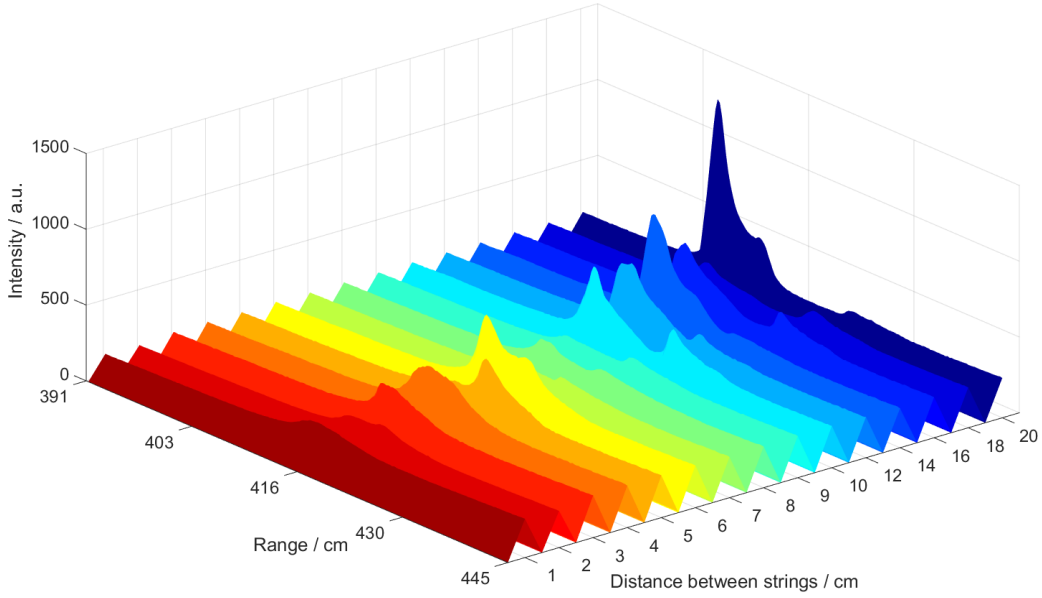

Figure 3.11: *Range resolution in the center of the probe volume. Different colors correspond to different distances.*

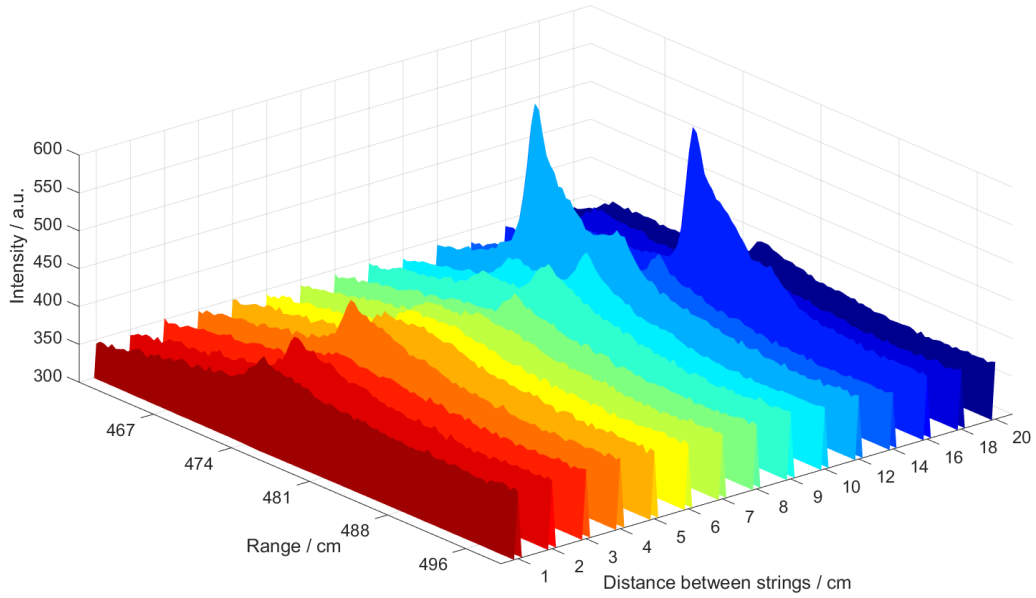

Figure 3.12: *Range resolution in the far end of the probe volume. Different colors correspond to different distances.*

There seems to be a focusing problem in the detector optics. When adjusting the collecting lens in such a way that the light is focused at the slit, a moon shaped pattern appears on the detector, as shown in figure 3.13. A smaller spot can be achieved on the detector by adjusting the collecting lens slightly, this does however lead to signal loss.

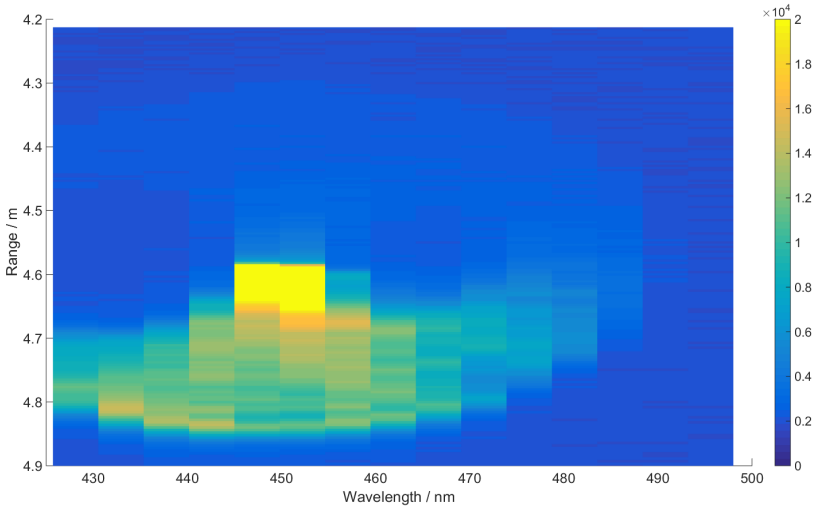

Figure 3.13: *Half moon shaped pattern that appear on the detector when the collecting lens focus is optimised on the slit.*

3.4 Modulation & ramp time

A Johnson counter made by Elin Malmqvist was installed between the trigger out gate on the detector and the trigger in gate on the laser to achieve a modulated signal. The strobe signal from the detector triggers the counter which turns the laser on and off every other exposure. A background image is thus obtained when the laser is off. This modulation makes it possible to subtract the background for every exposure where the laser is turned on. The modulation time is thus controlled by the exposure time, and the laser is triggered by the camera. Since the *Daphnia* were attracted to the laser light, as explained in section 5.3, a pause time between every duty cycle was introduced in order to make the method less intrusive.

When it was observed that the laser was unstable and did not emit a constant light intensity during the cycles, a ramp time was introduced. This was made by increasing the exposure time of the first two images in a cycle (one "off" and one "on", due to programming facilitation), in order to heat up the laser and obtain a more constant signal during the rest of the duty cycle. To find a suitable ramp time, several different combinations of ramp and exposure time were investigated. An example of the problem with too short ramp time is illustrated in figure 3.14 were the mean intensity in the elastic channel serves as an indicator of the laser power. In the ramp time tests, a 60 s pause time between the duty cycles was employed to allow the laser to cool down.

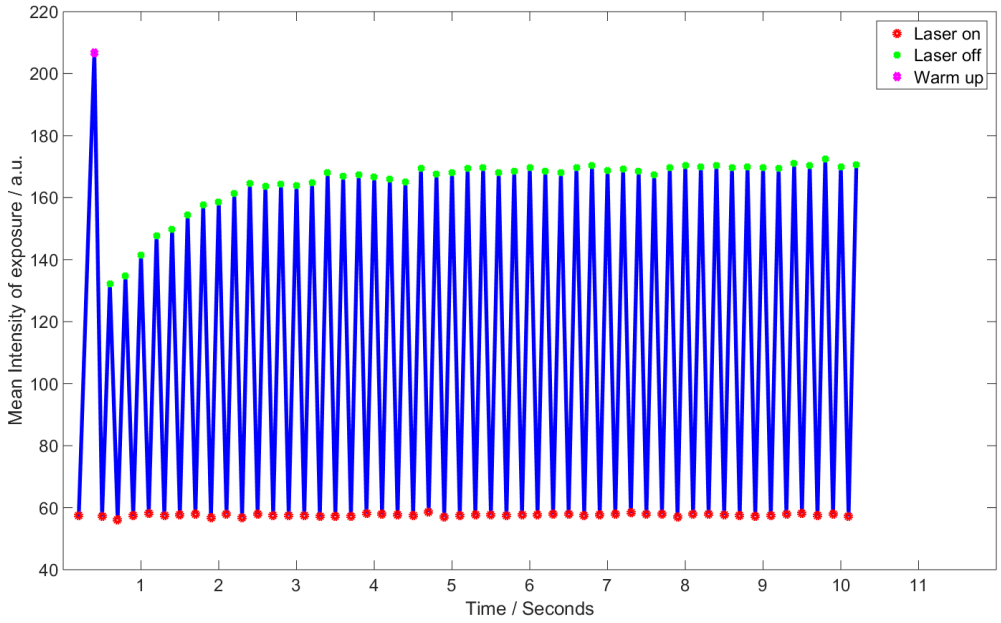

Figure 3.14: *The mean intensity of the elastic channel plotted for 100 exposures. The configuration in this example was a 200 ms ramp time and 100 ms exposure time.*

In figure 3.15, the mean intensity of the exposures where the laser was turned on is plotted against the exposure number, for three duty cycles. With an exposure time of 100 ms, a warm up time of 1 s is sufficient to achieve a constant laser power. The required warm up time is also dependent on the exposure time, a longer exposure time gives the laser time to cool down during the "off" exposures and more exposures are required before the laser power is stabilised.

The laser warm up can be seen in figure 3.15, where the data from 400 µs warm up time and 50 ms exposure time (cyan diamonds) are very similar to the data corresponding to both 500 ms/1 s warm up time (blue diamonds/red circles) and 100 µs exposure time. Interestingly, a longer warm up time than 1 s seems to cause the opposite problem, were the power decreases during the first exposures. This is in line with the other results which shows that the laser has a higher temperature in continuous mode than when it is modulated. Eventually, a 100 ms exposure time was chosen along with 1 s warm up time during most of the periodic experiments.

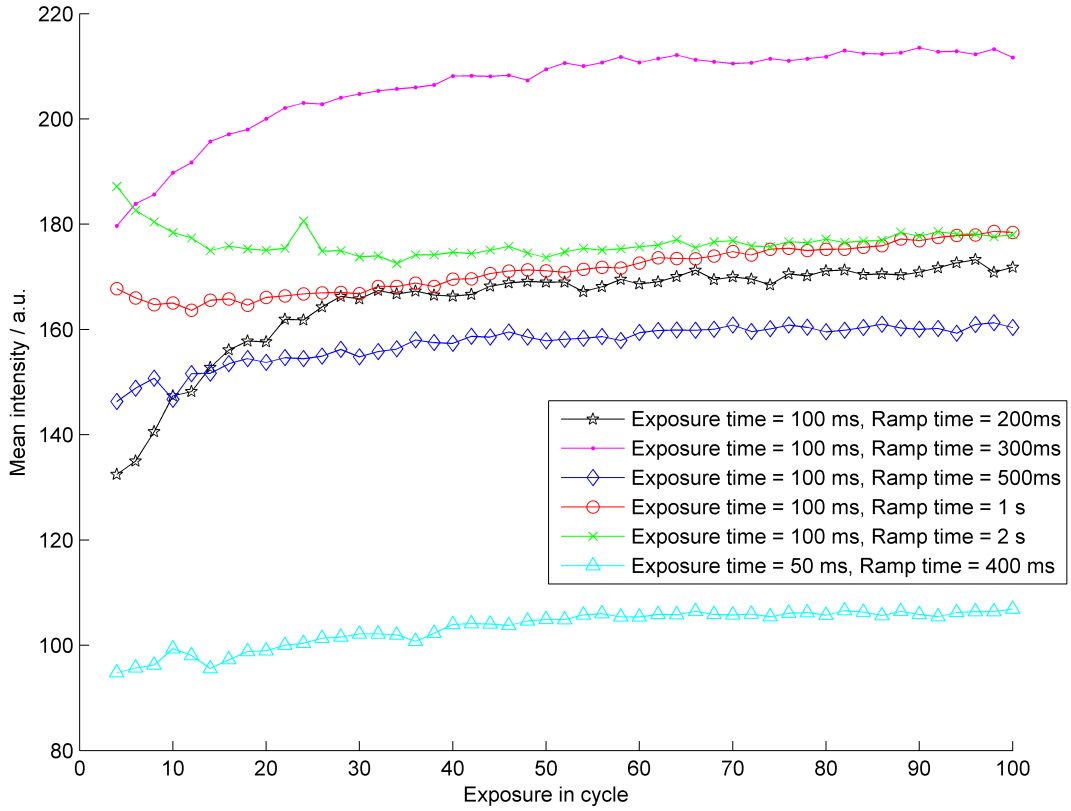

Figure 3.15: *Mean intensities over all range in the elastic channel for different ramp and exposure times, recorded over 3 duty cycles with 100 exposures in each cycle.*

4 Data analysis

The main program for the data analysis has, generally described, the following structure:

The data from the elastic channel is loaded from the folder, and assembled in a range-time matrix by the Matlab script `dataMatrixMaker`. `scanFile` then scans the range-time matrix for events by creating a binary map where the matrix elements of the events has the value 1 and the rest has the value 0. `extractEvents` creates a structure where each event is stored along with general information about the event, such as range interval, time, duty cycle number etc. The images from each event is then assembled and stored by `extractImages`, and `extractSpec` uses the images to calculate and store the wavelength spectra for the events. Finally, the spectra are analysed along with other event information in `evaluateSpectra`. A flowchart describing the data handling process is shown in figure 4.1. The structure and method of each part is described in the following sections.

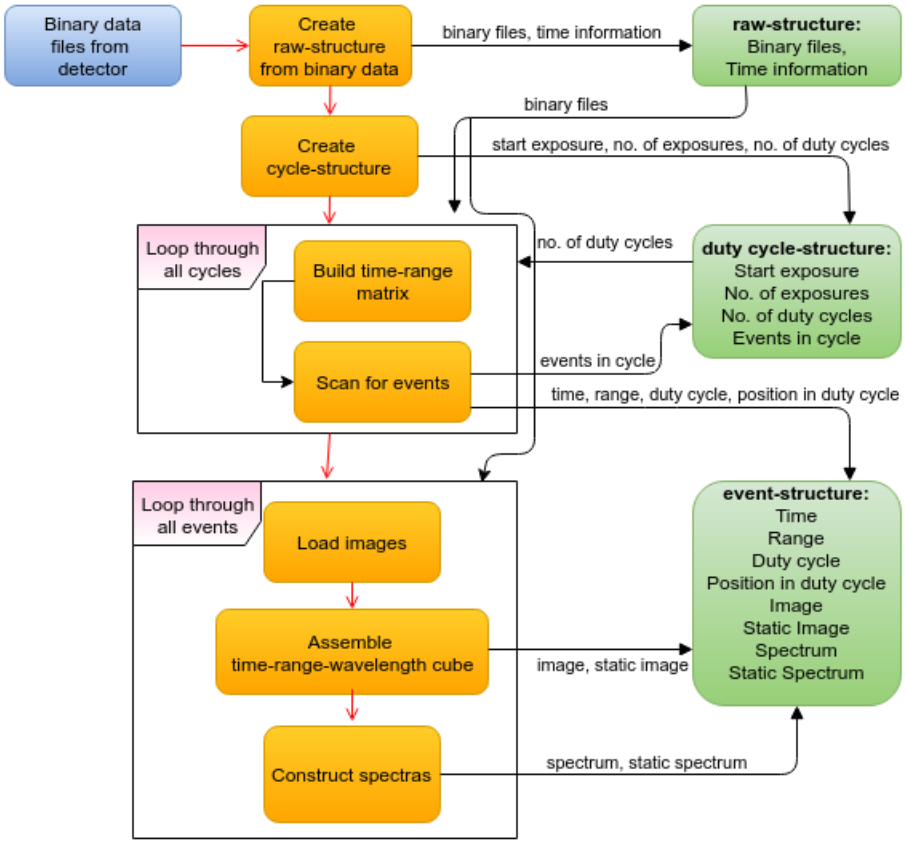

Figure 4.1: *Flow chart describing the extraction of detector images and spectra when the setup was in periodic mode.*

4.1 Data handling and matrix generation

The experimental setup generates roughly 75 kB per exposure, using binning by 8 on the wavelength pixels resulting in 61 spectral bands. This translates to 7.5 MB per period for the long running dispersal experiments. Typically, these experiments ran for 600-700 periods, generating 60 000-70 000 images and 5-6 GB of data. The data evaluation program was therefore constructed to keep the memory load on the computer as low as possible.

The camera produces images in 8-bit binary files which were are loaded by the Matlab script `dataMatrixMaker`. To avoid loading unnecessary data, initially only the binary files corresponding to all range values in the elastic channel are read. This data is used to assemble a large range-time matrix (as the example in figure 4.2a). If the laser has been modulated, the dark exposures are subtracted from the "laser on"-exposures and the exposures from the warm-up are removed by the scipt `cleanMatrix`. The resulting `dataMatrix` is then used for the event localisation.

4.2 Event localisation

Using the work from Malmqvist et.al [43], the dataMatrix is scanned for events. An example of a dataMatrix image is shown in figure 4.2a. It contains a strong event between 15:30:39 and 15:30:40 which causes a signal significantly stronger than the other peaks in the beginning and end of the data set (all at approximately 4 m range).

The minimum, maximum and median values along the range axis in the range-time matrix is calculated by the script `scanFile`. The minimum values serves as the noise "floor" in the data set whereas the median value represents the static backscattering signal from the water. The median range curve is chosen as static signal rather than the mean range curve since it is more insensitive to extreme values from events. A threshold for each range value is then created by folding the minimum curve over the median curve and multiplying by a signal-to-noise ratio.

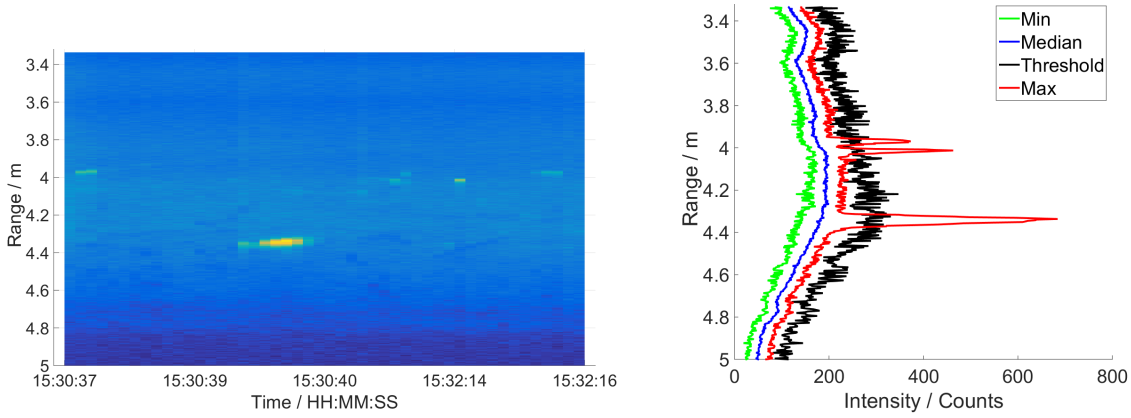

(a) *Sample of range-time matrix.* ***(b)*** *Intensity curves.*

Figure 4.2: *Example image and its associated values along the range axis. The events at 15:30:37, 15:30:39 to 15:30:40 and 15:32:14 in (a) rise above the threshold in (b). Using the signal-to-noise ratio 2.5, only these events are registered.*

A logical matrix of the same size as the range-time matrix is created by comparing each range-time point with its associated threshold. A value above the threshold becomes 1 and a value below becomes 0. To remove events that are too short in time or range to be analysed, the binary map is eroded by, in this case a [2x1] matrix. The eroded matrix is then expanded by a [15x2] matrix to make sure that one event does not get counted multiple times. The mask for the event in figure 4.2 is shown in figure 4.3a. The event is then stored with its corresponding range and time coordinates in an event structure by the scipt `extractEvents` before the next range-time map is loaded and the process is repeated until all data has been read.

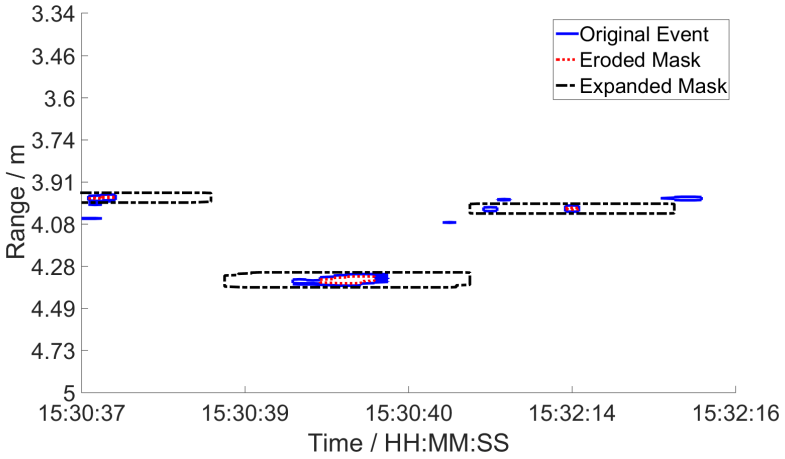

(a) Original, eroded and expanded masks.

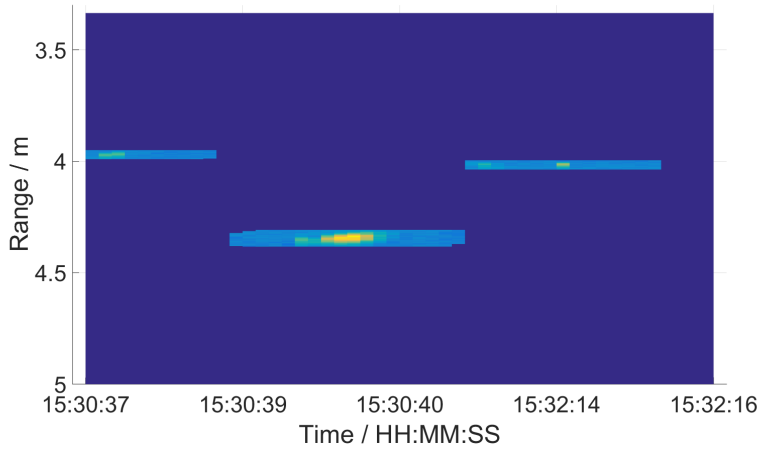

(b) The range-time matrix after the logical map been applied.

Figure 4.3: *Creation of the binary map and its application to the range-time map.*

4.3 Image loading and spectral construction

When the time coordinate of each event is known, a data cube with range-wavelength-time information is generated by the script `extractImages`. The cube is assembled from the binary files, exposure by exposure. The raw data comes in an array, and all range values in each spectral band is extracted one by one and placed next to each other as columns, constructing the detector image. All images are then placed after each other forming the data cube.

For each event, an event image, containing the temporal mean of the range-wavelength information during the event time coordinates is saved in the event structure along with a static image. The static image consists of the temporal median of the range-wavelength values in the whole data cube. The event image for the example event shown earlier in section 4.2 is displayed in figure 4.4a along with its corresponding static image in figure 4.4b. To only obtain the wavelength spectrum of the event, the static signal is substracted from the event image, as shown in figure 4.4c. To achieve a representative static signal, the time over which the temporal median signal should be obtained has been investigated for each measurement and changed depending on the measurement conditions.

The script `extractSpect3` constructs the wavelength spectra for each event by taking the mean signal over the range of the event in the event image. The range of the event is stored with the event during the extraction from the range-time matrix as described in section 4.2 and is marked with a red box in the detector images in figure 4.4. The corresponding spectrum from the static image is then subtracted from the spectrum. The event spectrum, the static spectrum, and the final spectrum are shown in figure 4.4d where the final spectrum (i.e. event spectrum subtracted by static spectrum) is used for further analysis.

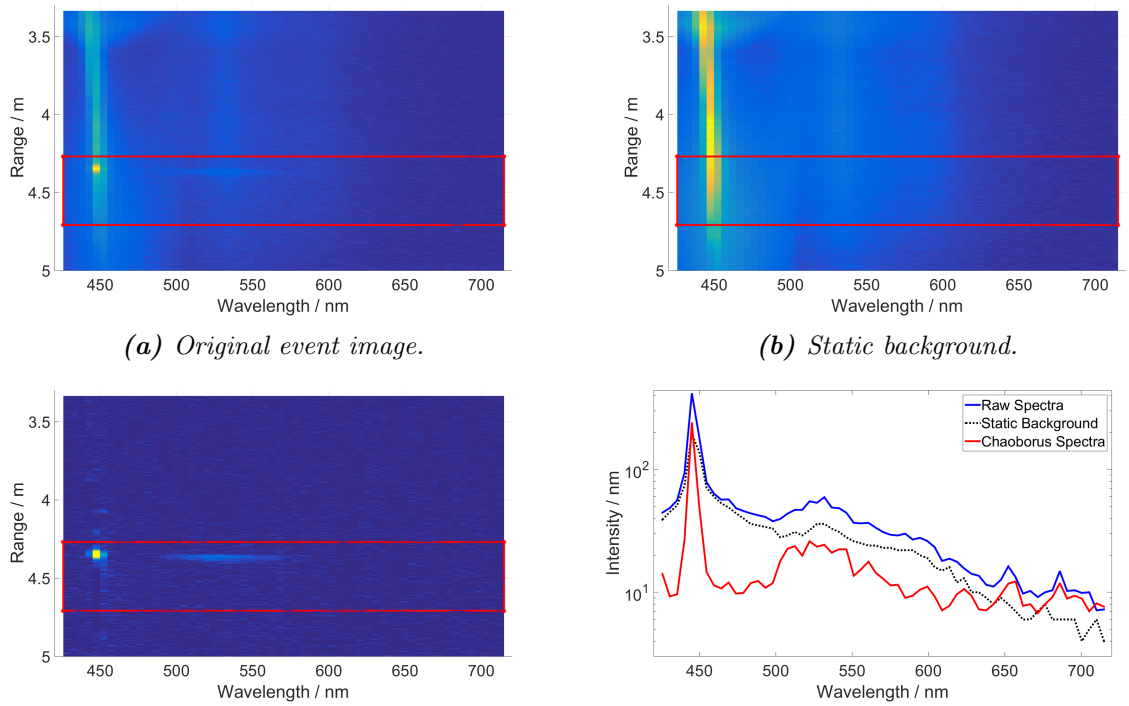

(a) *Original event image.*

(b) *Static background.*

(c) *Event image with background subtracted.*

(d) *Calculated spectra from images (a), (b) and (c).*

Figure 4.4: *Event images and spectra. The event range is marked with red lines in image (a), (b) and (c). The original spectrum is the mean signal over the marked range whereas the static background consists of the temporal median signal over the same range. The intensity has arbitrary units (counts) in all images.*

4.4 Differences between modulated, periodic and continuous laser data

The setup can be used for continuous duty cycle with and without laser modulation, and also periodic measurements with a pause time between each duty cycle. This leads to additional requirements on the data handling process. If the laser is modulated and every second exposure is taken with the laser off, the main difference from the continuous mode is that every second exposure should be subtracted from the following exposure. This does not cause any major changes to the program; it is still possible to change the size of the range-wavelength-time data cube arbitrarily, and the time between each exposure is always the same (i.e. one exposure time).

When the setup is in periodic mode, as during most of the longer dispersal experiments, greater care needs to be taken. Figure 4.5 shows a setup with 100 exposures per duty cycle, were the first exposure is an "off" exposure of 1 s (due to programming facilitation), the second exposures

is the ramp time exposure of 1 s, and the others have an exposure time of 100 ms. A pause time of in this case one minute between each duty cycle is introduced to obtain a low duty cycle.

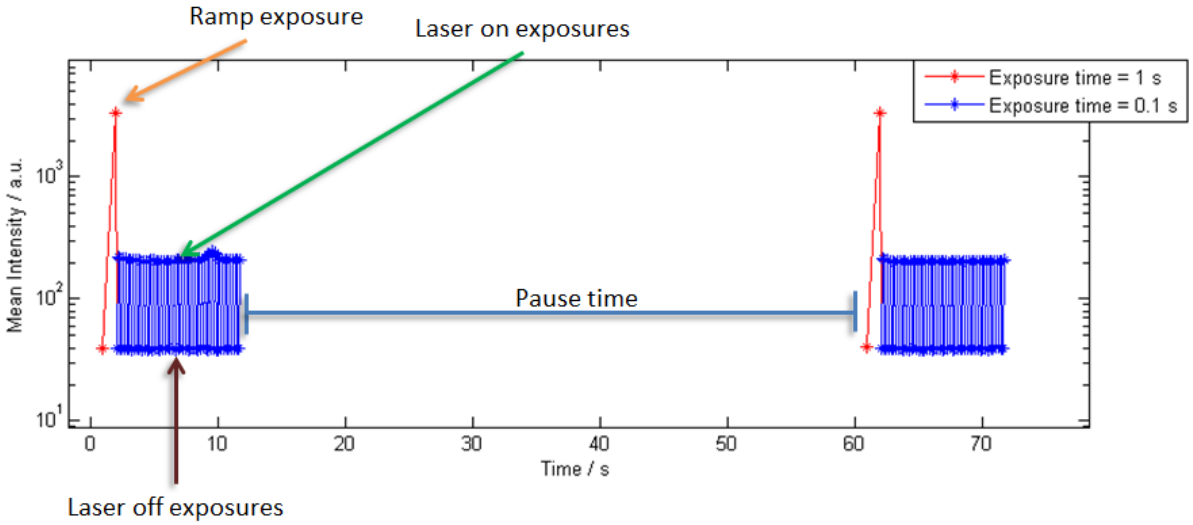

Figure 4.5: *When the laser runs in periodic duty cycles with varying exposure time within the duty cycle the time between two exposures can vary significantly. The mean intensity for the exposure is plotted in the y-axis. With an exposure time 10 times longer, the mean intensity is correspondingly one order of magnitude higher.*

When the setup was in periodic mode, all the range-time matrices in each duty cycle were scanned one by one to prevent the script from clustering events from different duty cycles. Similarly, one range-wavelength-time cube was also loaded for each duty cycle. For improved memory performance, the data cubes were temporarily stored in the duty cycle structure and not reloaded for each event. After the final event in a duty cycle was investigated, the data cubes were removed from the memory. This allowed for investigation of a large amount of data without requiring all data to be stored in the RAM memory simultaneously.

4.5 Data analysis of dyed animals

A method used in spectroscopy to find patterns in data and distinguish between different wavelength spectra is the use of Singular Value Decomposition (SVD) followed by Hierarchial Clustering Analysis (HCA). In this context SVD and HCA provided a means to differentiate between the wavelength spectra of two species of aquatic fauna when coloured with different dyes (as described in sections 5.2 and 5.4).

4.5.1 Singular Value Decomposition

Singular Value Decomposition (SVD) is a way to reduce the data amount by linearly decomposing the spectra into spectral components, and ordering them by their significance. The SVD of the data matrix $\mathbf{A}$ is the matrix product

$$\mathbf{A} = \mathbf{USV}^T. \tag{13}$$

In SVD, one finds a subspace of $\mathbf{A}$ with lower dimension that best represents $\mathbf{A}$. This means minimizing the sum of the squares of the perpendicular distance to the set of data points. An advantage of SVD is that one can ignore variation below a certain threshold and thus reduce the amount of data significantly, as shown in figure 5.13a. [44] [45]

Four matrices are involved in the SVD:

- $\mathbf{A}$ is the raw data matrix of size $m \times n$, where in this case m is the number of wavelength spectra (i.e. number of events) and n is the number of spectral bands:

$$\mathbf{A}_{m,n} = \begin{pmatrix} \lambda_{1,1} & \lambda_{1,2} & \cdots & \lambda_{1,n} \\ \lambda_{2,1} & \lambda_{2,2} & \cdots & \lambda_{2,n} \\ \vdots & \vdots & \ddots & \vdots \\ \lambda_{m,1} & \lambda_{m,2} & \cdots & \lambda_{m,n} \end{pmatrix} \tag{14}$$

  As an example, $\lambda_{1,1}$ is the first spectral band of the first event, $\lambda_{2,1}$ is the first spectral band of the second event and so on.

- $\mathbf{V}$ contains the set of orthonormal eigenvectors with associated eigenvalues $\{\mu_1, \mu_2, ..., \mu_n\}$ to the $n \times n$ matrix $\mathbf{A}^T\mathbf{A}$. :

$$\mathbf{V}_{n,n} = \begin{pmatrix} v_{1,1} & v_{1,2} & \cdots & v_{1,n} \\ v_{2,1} & v_{2,2} & \cdots & v_{2,n} \\ \vdots & \vdots & \ddots & \vdots \\ v_{n,1} & v_{n,2} & \cdots & v_{n,n} \end{pmatrix} \tag{15}$$

$$(\mathbf{A}^T\mathbf{A})\mathbf{v}_i = \mu_i\mathbf{v}_i \tag{16}$$

  The i:th eigenvector $\mathbf{v}_i$, called principal component i, make up the i:th column of $\mathbf{V}$.

- $\mathbf{U}$ contains the set of orthonormal eigenvectors to the $m \times m$ matrix $\mathbf{A}\mathbf{A}^T$:

$$\mathbf{U}_{m,m} = \begin{pmatrix} u_{1,1} & u_{1,2} & \cdots & u_{1,n} \\ u_{2,1} & u_{2,2} & \cdots & u_{2,n} \\ \vdots & \vdots & \ddots & \vdots \\ u_{m,1} & u_{m,2} & \cdots & u_{m,m} \end{pmatrix} \tag{17}$$

  The i:th eigenvector $\mathbf{u}_i$ make up the i:th column of $\mathbf{u}$, and contains information about the weight of each principal component for each event. As an example, $u_{1,1}$ is the weight of the first principal component on the first event, $u_{2,1}$ is the weight of the first principal component on the second event, and so on.

- $\mathbf{S}$ is a diagonal matrix, containing the singular values σ_i in descending order, defined as:

$$\sigma_i \equiv \sqrt{\mu_i}. \tag{18}$$

  The singular values satisfy the following two relations:

$$\mathbf{A}\mathbf{v} = \sigma\mathbf{u} \tag{19}$$

$$\mathbf{A}^T\mathbf{u} = \sigma\mathbf{v} \tag{20}$$

  The singular values specifies the significance of the principal components when representing the original data. Since they are ordered in descending order, the first principal component has the most significance.

When the decomposition is done, the data can be reduced by truncation, and the weight information of each principal component contained in **U** is used for further analysis to discriminate the different spectra using HCA. [45] [46]

4.5.2 Hierarchial Clustering Analysis

By using HCA in combination with SVD, it is possible to discriminate the different spectra. In HCA, the **U** and **S** obtained from the SVD is used. A space is created which are spanned by a chosen number of vectors (components) in **U** (the rest are discarded by the truncation). The points in **U** are then grouped by the euclidean distance from each other in the "**U**-space". This grouping can be visualised if choosing either two or three vectors and plotting them as a 2D- or 3D-plot (as shown in figure 5.13c). By comparing the spectra in each group with a "signature spectrum" from in this case a dyed *Daphnia* and *Chaoborus* respectively, the events from the two different animals can be separated.

5 Experiments & Results

5.1 Aquatic experimental setup

Figure 5.1 shows the experimental setup with the tank and LIDAR system. A water tank with dimensions 5.00x0.37x0.30 m (LxWxH) was used, covered with black paper on the outside to remove background radiation. Black fabric was put on the inside wall of the tank, on the side of the field of view of the detector, to remove reflections from the tank wall. As beam termination, either a beam dump or black antistatic foam was used, depending on what experiment was performed. The LIDAR system was placed on a wooden board, facing the short side of the tank, and was covered by black neoprene and paper to shield from background light. The laser beam was convergent and focused at the beam termination.

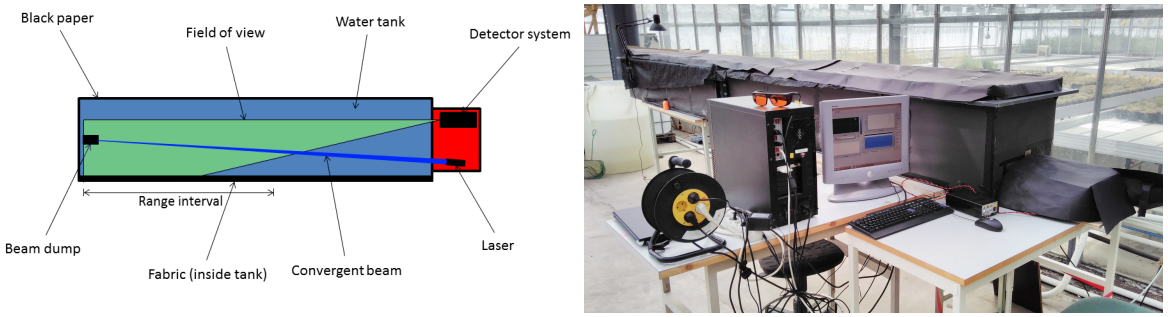

(a) Schematic figure of the experimental setup, (b) Photograph of the covered experimental setup. seen from above.

Figure 5.1: *Schematics and photograph of the experimental setup. The laser and detector are covered with several layers of black neoprene and paper.*

5.2 Dye colouring

No auto-fluorescence signal could be achieved from the *Daphnia*. Therefore different methods of labelling them with fluorescent dye were employed, to be able to distinguish between species in later experiments. Labelling with quantum dots, which is a standard method for zooplankton, was not used because of the high cost. Attempts were made with Fluorescein 27, Fluorescein Sodium and Rhodamine 6G, but since they were not properly dissolved in water, they were not used in further experiments. Tests performed with dyes from fluorescent marker pens showed promising results, and they were easy to obtain and handle. A sample of the dyes used during the experiments, recorded using a pipette submerged in the tank and inserted in the laser beam, is presented in figure 5.2.

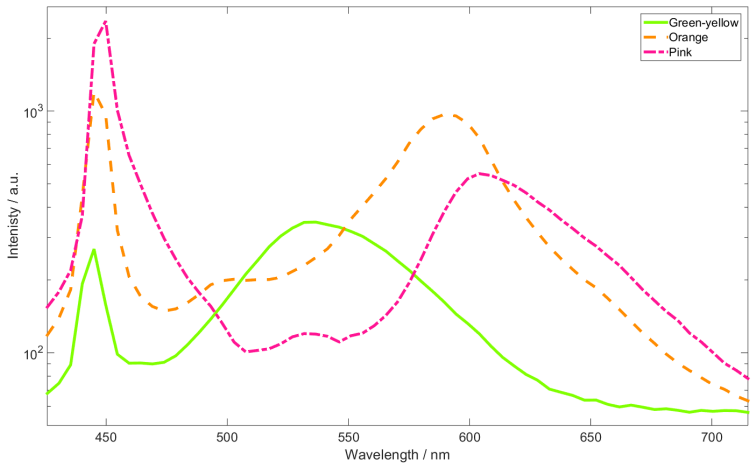

Figure 5.2: *Spectra from the marker pen dyes used during the experiments. Pink and orange dye both mostly fluoresce yellow.*

In figure 5.2, it is clear that all investigated dyes to some degree overlap the Raman line at 523 nm. This could cause problems during the spectral analysis unless the static signal is properly subtracted from the image. However, even in the untreated raw data it is possible to resolve the spectral features to some degree. An example is presented in figure 5.3 which contains a 3D-plot of two *Daphnia*. A weaker signal is present after 1 s at 3.9 m, followed by a much stronger signal 1 s later at 4.4 m. Both events increase the intensity in the elastic channel. In the Raman channel, the signal increases with distance due to the range/pixel relation and the increased intensity in the toothpaste-shaped laser beam which was focused at the termination. The termination is seen as a solid tube in the elastic channel at 4.8 m. During the second event, a small extinction in the Raman channel can be seen.

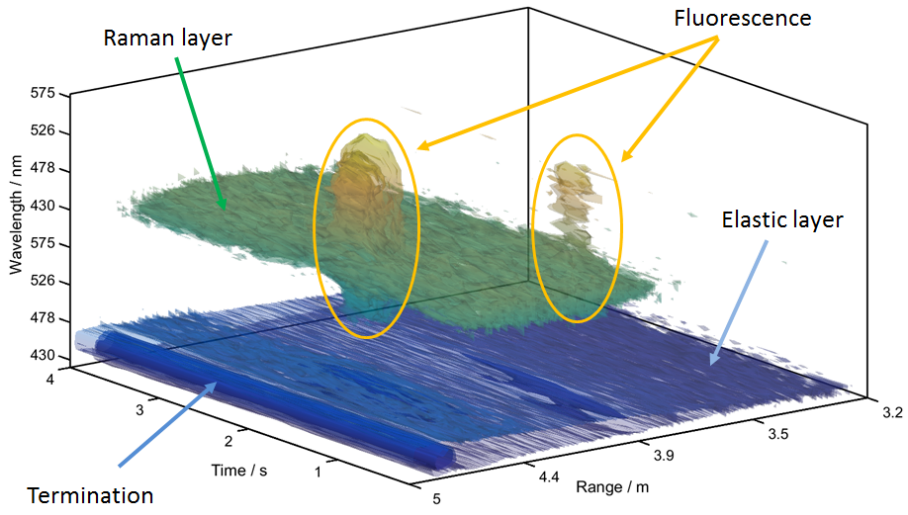

Figure 5.3: *3D-image of two consecutive Daphnia events. The fluorescence signal from Fluorescein 27 is overlapping the (green) Raman channel. The solid termination target is seen as a strong signal at 4.8 m in the (blue) elastic channel.*

The influence of the size of the *Daphnia* on the quality of the dyeing was investigated. Small and large *Daphnia* were separated manually and coloured. Both groups were then released into the tank and monitored for 20 hours. The setup registered 1440 events where only 4 *Daphnia* could be identified as dyed pink and 39 dyed green, the final 1397 events could not be identified. The mean spectra for the small, large and for all events are presented in figure 5.4. The large *Daphnia* caused stronger backscattered signal, than the smaller *Daphnia*. Comparing the mean intensity over three spectral bands around the elastic peak, the signal is 50 % higher for the group of large *Daphnia* compared to the group of smaller *Daphnia*. Both these signals are however much larger than the mean signal strength for all events. This indicates that a very strong signal is required for the fluorescent light to be recorded but could also indicate that most *Daphnia* are too small to be successfully dyed using dye from marker pens.

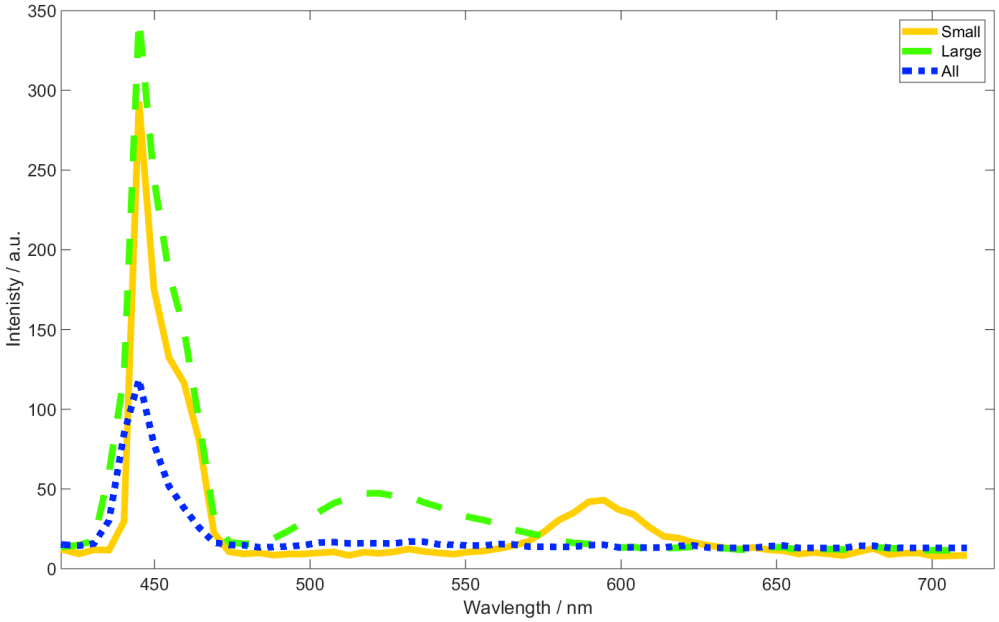

Figure 5.4: *The Daphnia size greatly influences the fluorescence of the organism. Large Daphnia were dyed green and yielded the strongest elastic signal, small Daphnia were dyed pink and cause a weaker signal. The mean spectrum of all Daphnia does not show any fluorescence features and has very low intensity in the elastic channel.*

5.3 *Daphnia* dispersal

The aim with this experiment was to see how the *Daphnia* were dispersed when released at the same initial location. The initial condition was set by covering the top of the tank with black paper so that no background light could enter the tank, and then a flashlight was directed into the tank from above at a specific location. The light from the flashlight attracted the *Daphnia* so that they formed a column underneath it, and when the experiment started the flashlight was turned off. This experiment was performed both with and without background light (i.e. both without and with paper covering the top of the tank), and the experimental setup for both experiments is shown in figure 5.5. The laser was operating continuously, i.e. no modulation was implemented.

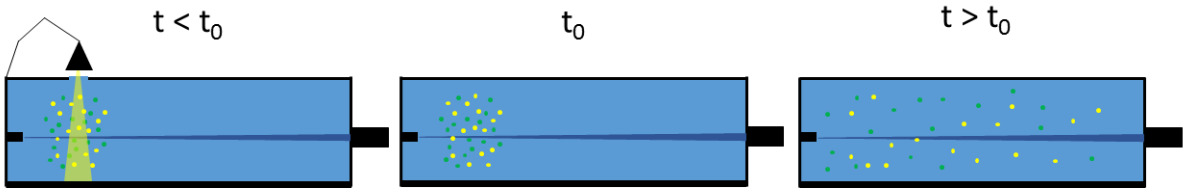

(a) Without background.

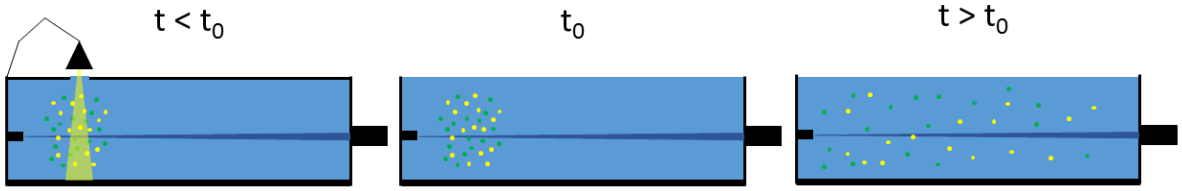

(b) With background.

Figure 5.5: *Schematic figure of the experimental setup, seen from the side. The initial condition was set by covering the tank and directing a flashlight into a hole in the top of the tank. In the experiment with no background (5.5a), the flashlight was turned off and the hole covered at t_0. In the experiment with background (5.5b), the flashlight was turned off and the lid covering the top of the tank was removed at t_0.*

Figure 5.6 shows the dispersal of *Daphnia* in the water tank. It is clear that the *Daphnia* are attracted by the laser light source, since they moved towards shorter ranges (i.e. towards the detector) faster with increasing exposure to the laser radiation. During the following experiments, a duty cycle of approximately 10 s and a minimum of 60 s pause time was chosen since it seemed sufficient for the *Daphnia* to forget the laser position.

With 15 s pause time between the duty cycles, the *Daphnia* reached the lower edge of the probe volume in roughly 8 minutes, corresponding to an average swimming velocity of 20 cm / minute. With no pause time, the *Daphnia* reached the edge twice as fast, corresponding to a swim velocity of 40 cm / minute. This can be compared to earlier studies which finds the average swim velocity of *Daphnia* in presence of predatory fish to be 48 cm/min [47].

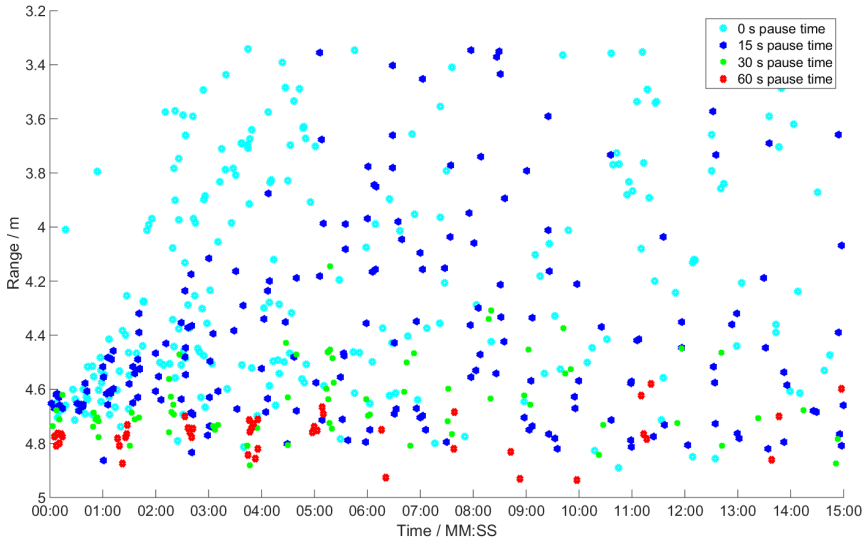

Figure 5.6: *The positions of detected Daphnia for different pause times between the laser duty cycles.*

With 30 and 60 s pause time, the *Daphnia* did not spread out as much in the tank. This could indicate that the complete lack of light disorients the *Daphnia* since, when the lid is removed from the tank, the dispersal rate is very similar to the experiment with no pause time (as seen in figure 5.7). Although the results are similar, there is one important difference. When all background light is removed, the *Daphnia* assembles at the laser source, but when the lid is removed the *Daphnia* disperse towards the edges of the tank and do not gather at the laser source.

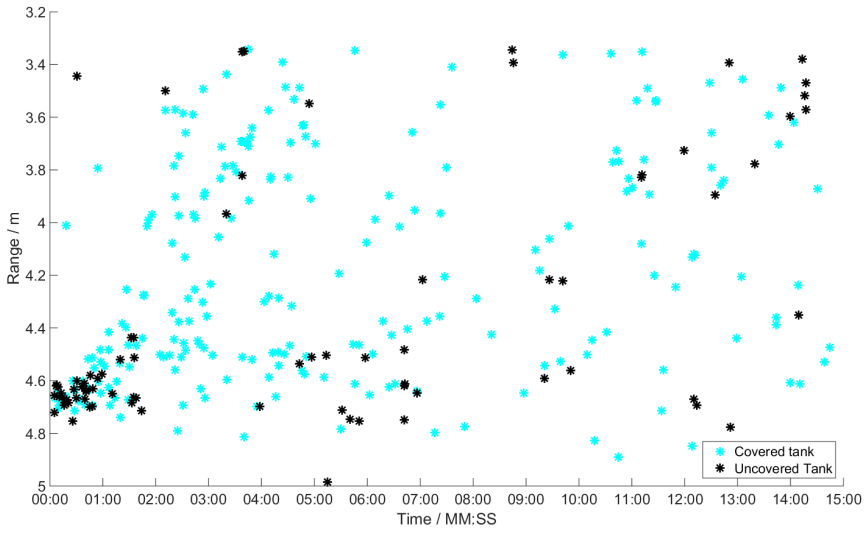

Figure 5.7: *The positions of detected Daphnia with and without a covered tank.*

5.4 *Daphnia* & *Chaoborus* dispersal

The initial aim of this experiment was to observe interaction kinetics between the two genera *Daphnia* and *Chaoborus*. The experiment was performed three times under different conditions before a reliable result was obtained.

5.4.1 *Daphnia* & *Chaoborus* experiment 1

The *Daphnia* were dyed with Rhodamine 6G and the *Chaoborus* with Fluorescein 27. The animals were put in containers with the dye dissolved in water for a couple of hours, and then they were collected using a net and rinsed with clean water. The laser was configured to run in intervals of 100 exposures with 100 ms exposure time, with an initial warm up time of 750 ms and a 90 s pause between each interval.

The *Daphnia* and *Chaoborus* were gathered in the water tank using a flashlight (as illustrated in figure 5.5a) for ten minutes in the middle of the range interval before the whole tank was covered. The experiment ran for approximately 17 hours. After the experiment was finished, it was discovered that the tank had been contaminated by undissolved Fluorescein 27 which rendered the experimental data useless. Very few *Daphnia* were however found at the laser source and the experimental setup was overall deemed successful, though on closer inspection, the problem with laser warm up had persisted.

Only 145 events were found in this experiment and the tank became contaminated by undissolved dye. Therefore, no extensive analysis could be performed on the data initially. With improved suppression of the static signal, it eventually became possible to retrieve some data which is presented in figure 5.8. Group 1 and 4 contains 4 events together and are very likely from *Daphnia* since they fluoresce orange. Group 5 fluoresce green and can therefore be identified as *Chaoborus* but only consists of 1 event. Group 3 contains 4 events and have a broader spectra than the other groups. Since the spectrum of group 3 overlap both the orange and green-yellow peak, it suggests that these spectra could be the result from a "double hit" with both *Daphnia* and *Chaoborus* in the beam. However, the peaks originate from the same point in the tank so if they are from two different objects, they are very close to each other. Another explanation could be that the spectra are from Fluorescein dye particle which could have floated into the beam. Group 2 is the largest group with 136 events which only contains elastic scattering.

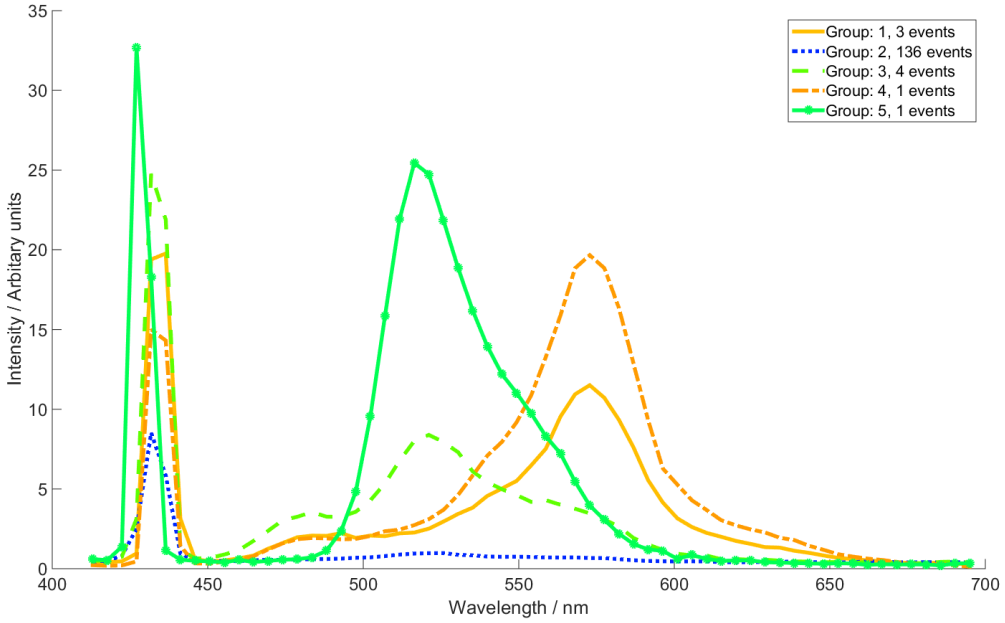

Figure 5.8: *Spectra from the first experiment. Solid dye was used to mark the Chaoborus which contaminated the tank. The spectra are clustered using HCA as explained in section 4.5.2.*

5.4.2 *Daphnia* and *Chaoborus* experiment 2

To avoid contamination of the water tank, only liquid dye from marker pens was used when dying the *Daphnia* and *Chaoborus*. The *Daphnia* and *Chaoborus* were dyed with orange and yellow dye, respectively. The laser configuration was similar to the configuration described in section 5.4.1, the only difference being the laser warm up time which was increased to 1 s to completely avoid the laser warm-up problem.

Daphnia and *Chaoborus* were again gathered using a flashlight for ten minutes before the tank was fully covered and the experiment started. The experiment ran for approximately 18 hours. After the experiment was finished, a large amount of dead *Daphnia* were found on the bottom of the tank. This might have been due to a to high water pressure during rinsing or a too high concentration of *Daphnia* during dying.

Since only 354 events were found in 17 hours, no clear conclusions can be drawn from this experiment. The spectra, coloured according to their HCA classifications are shown in figure 5.9. Group 3 consists of 9 events with a single peak at the green-yellow position and a strong elastic signal and the group is very likely to contain *Chaoborus* events.

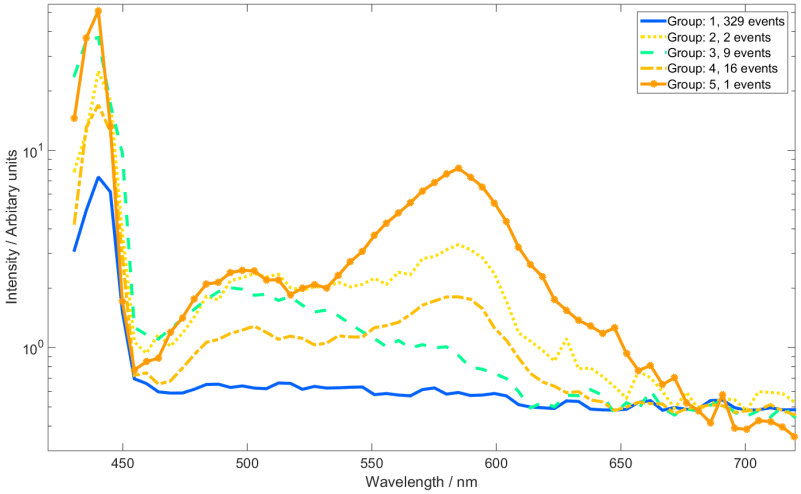

Figure 5.9: *Spectra from the second experiment. The solid dye was changed to liquid marker pen dye but very few events were recorded.*

The spectra from group 5, 4 and 2 are very similar but with different fluorescence peak intensities. These 19 events are very likely to originate from *Daphnia* since their largest peak lies at 600 nm and the orange dye hump is clearly seen at 500 nm. The majority of the events does not contain any significant spectral information and were placed in group 1. They are probably *Daphnia* or free floating particles.

5.4.3 *Daphnia* and *Chaoborus* experiment 3

The *Daphnia* were labeled with dye from pink marker pens, and the *Chaoborus* with green - yellow colour to achieve a greater spectral difference between the different kinds of events than before. The experimental setup is shown in figure 5.10. The laser configuration was the same as in section 5.4.2 but to detect more events and gather the *Daphnia*, a small hole was cut into the lid of the tank in the middle of the range interval. The experiment ran during 20 hours from afternoon to mid day and the change in background illumination caused a clear change in *Daphnia* behaviour.

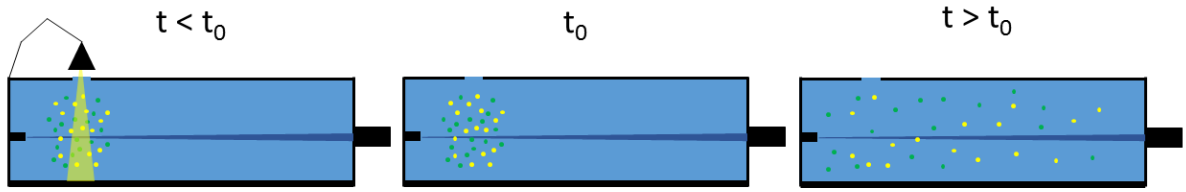

Figure 5.10: *Schematic figure of the experimental setup, seen from the side. The initial condition was set in the same way as earlier experiments, but this time the hole was left opened during the entire experiment.*

A more conscientious, but time consuming technique was employed during dyeing and rinsing for this measurement. A net was placed on top of the dye jar and water was then carefully poured into the jar from above, causing it to overflow and slowly rinse the *Daphnia*. The rinsing continued until no dye could be seen in the dye jar. This method was successful since no *Daphnia* seemed to die during the marking process and 3853 events were recorded during a 21-hour long experiment. The major increase of events were both due to an increased amount of *Daphnia* and *Chaoborus* in the tank and also due to the hole in the lid.

As shown earlier in section 5.3, the *Daphnia* are, when isolated from stray light, heavily attracted by any light source. This is clearly seen in figure 5.11. This experiment was performed the 12th of April 2016 when the sunset, and thus the loss of most background light, occurred at 20:15. The *Daphnia* appear to move roughly 30 cm at this time. Two hours later, they completely scattered and became distributed evenly in the tank. At dawn, around 5 A.M, they start to regroup at the hole in the lid. The shift at 21:00 and 23:00 are probably due to the ceiling light which probably turns on and off at these times.

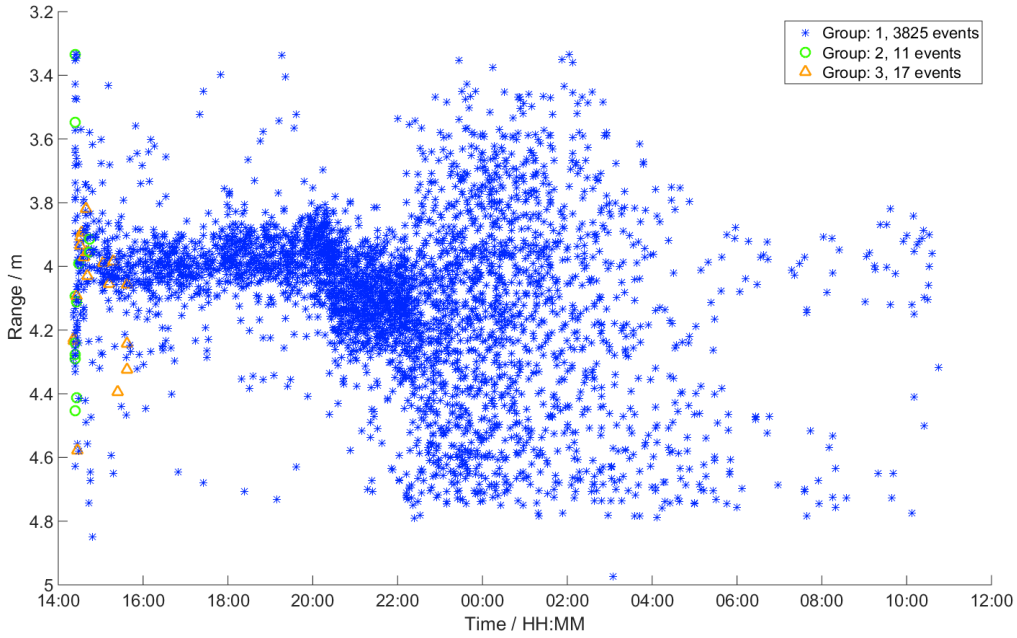

Figure 5.11: *Range time map over all found events. Symbol colours corresponds to the clustering presented in figure 5.12 and 5.13.*

In figure 5.12, the HCA and spectral analysis are presented. As seen previously, the absolute majority of the events does not exhibit any spectral features except in the elastic channel. The HCA was done with 10 principal components and 11 clusters. The number of principal components and HCA clusters was increased to achieve a higher dispersion of the spectra. The mean spectra for these 11 groups were then compared and clustered manually to 3 new groups. Group number 1 contains 3825 events without any significant spectral features. The majority of these events are likely to be small or unsuccessfully marked *Daphnia* since there were many more *Daphnia* than *Chaoborus* in the tank. Group 2 contains 11 events with green fluorescens and is therefore identified as *Chaoborus* and Group 3 contains 17 successfully dyed *Daphnia* events.

There is a periodic structure in the spectra with peaks separated by 25 nm. This is clearly seen in group 1 and to some degree in group 2 and 3. This phenomenon is not unique for this experiments but is an artifact in the detector and it appears to some degree in all experiments. Figure 5.14 shows the mean spectrum from all "laser off" exposures during the experiment where the peaks are clearly seen as well. The reasons for the appearance of the peaks have been investigated and is discussed in section 6.2.

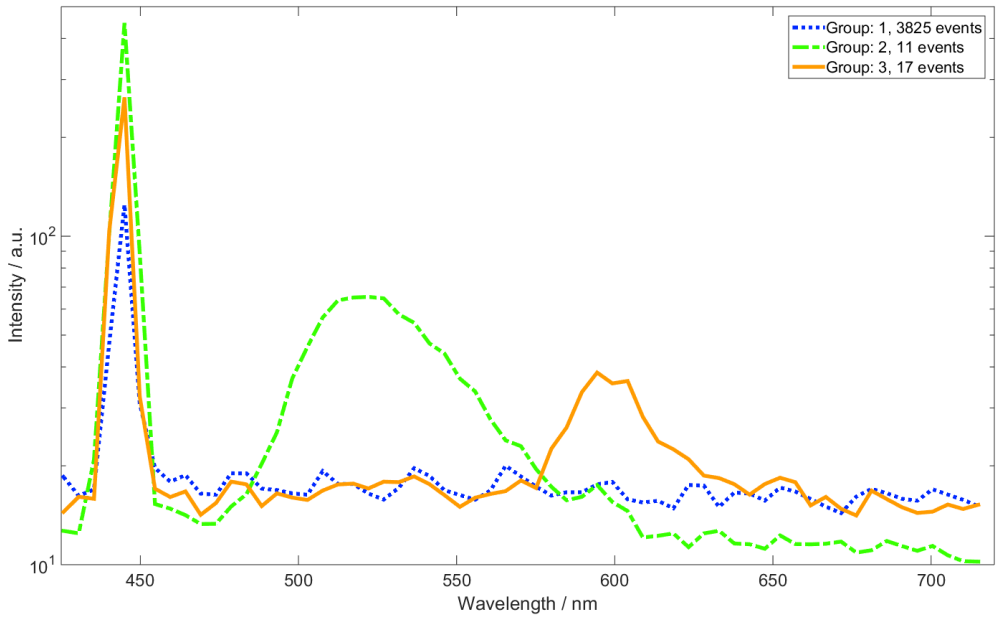

Figure 5.12: *Spectra for the third experiment after HCA and manual clustering.*

In figure 5.13c the events are plotted against the first 3 **U** vectors. In this figure, it is clear that some events in group 3 are very similar to group 1. To focus on the spectral features during the SVD and HCA, only 54 spectral bands were included in the analysis which excluded the elastic channel since it otherwise would dominate the clustering. The strength of the elastic signal is unsuitable for clustering since the amplitude of the elastic signal could vary with the orientation and position of the target in the laser beam. It can however be analysed and, eventually, used for e.g. size determination.

The dendrogram from the HCA clustering is presented in figure 5.13b and the result from the following, manual clustering is marked with corresponding colors. In both figure 5.13b and 5.13c, one can see that the similarities are larger between group 1 and 3 than between 3 and the other groups. This is natural since the majority of the events in group 1 is believed to be *Daphnia*. The HCA group 6 consits of the spectra that lie closest to the blue cluster in the **U**-space in figure 5.13c.

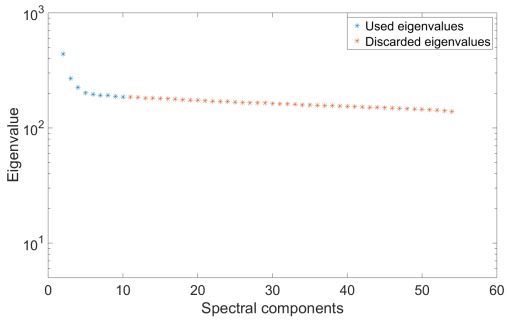

(a) Eigenvalues for the spectral components.

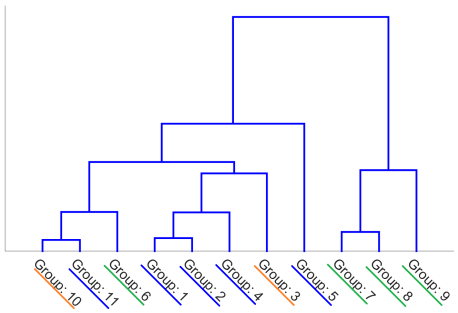

(b) Dendrogram

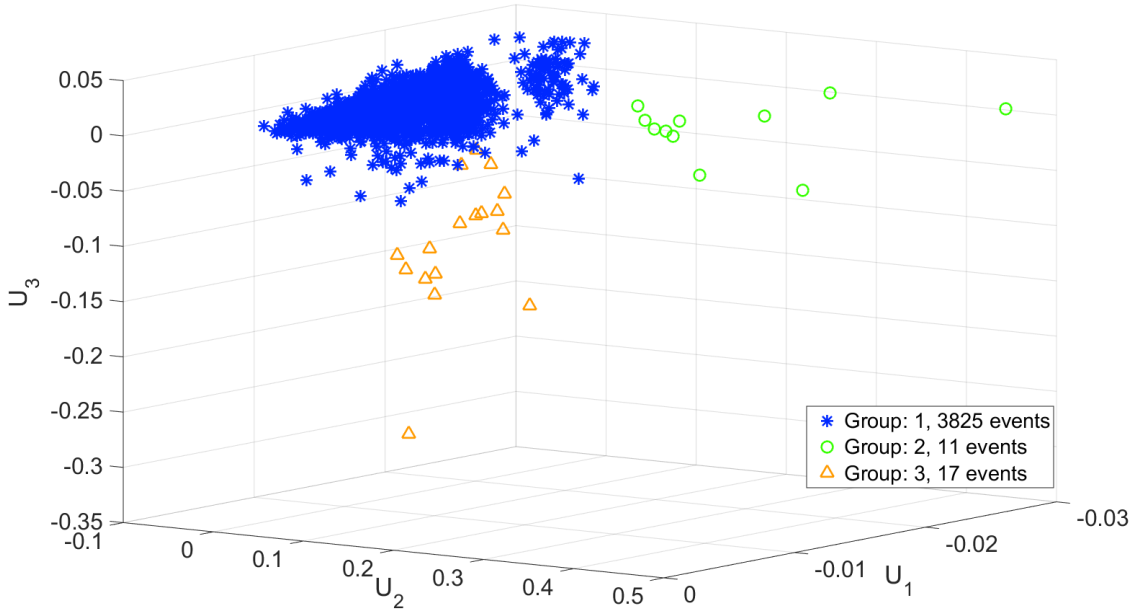

(c) All events plotted against the first three principal components.

Figure 5.13: *HCA performed using the 10 principal components whose eigenvalues are marked blue in (a) (the rest are discarded by truncation). The dendrogram in (b) illustrates the similarity between the HCA constructed groups and the result of the manual clustering plotted in (c). Group 1 is more similar to group 3 than to group 2.*

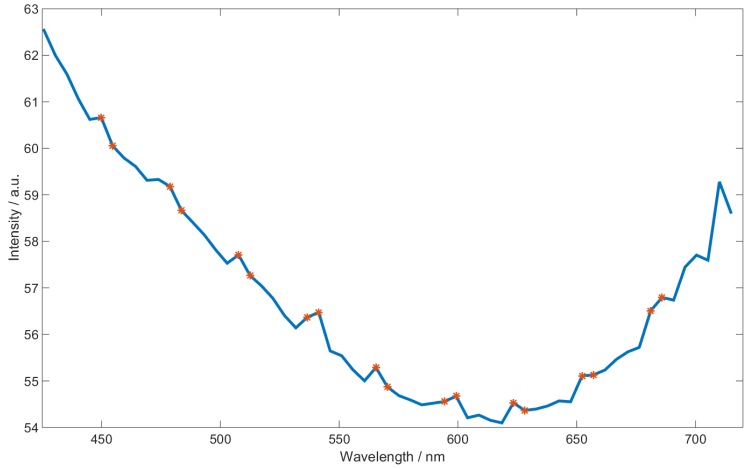

Figure 5.14: *The resulting spectra from background exposures taken with the laser turned off. The intensity in all images and ranges are added together for each spectral channel. The positions of the peaks appearing in figure 5.12 are marked with orange dots.*

5.5 Plant scanning

In this experiment, the target was a branch of a terrestrial plant, which was scanned in order to create a 3D-image. Since the LIDAR system can resolve one spatial dimension, information from the two other dimensions were obtained by moving the plant, in a similar manner as in whisk broom scanning. This was achieved by a LEGO robot, shown in figure 5.15. The robot drove approximately 60 cm forwards and backwards in 10 s, and then moved the arm, which held the plant, upward one step (0.5 cm). The process was repeated until the whole plant was scanned. Two vertical rods were set up on each side of the plant to mark the image borders (needed for reference when constructing the image from the raw data).

The laser was run in continuous mode with an exposure time of 10 ms, which can be compared to the 100 ms exposure time used in most aquatic experiments. The significantly shorter exposure time was needed to avoid saturation in the elastic channel since the backscatter intensity was much higher without the attenuation from water.

Figure 5.15: *A simple robot was constructed for smooth moving of the plant. A period consisted of a forward and backwards movement across the laser beam before the plant was raised 0.5 cm and the process repeated.*

A branch of a Thuja and its reconstructed 3D-model is shown in figure 5.16. The resemblance between the 3D-image and the branch could be improved by a smoother movement of the plant since swaying is a problem. Other plants were also scanned but with poorer result, mainly due to problems with the reconstruction of the images, which so far is done by manually selecting and arranging the exposures.

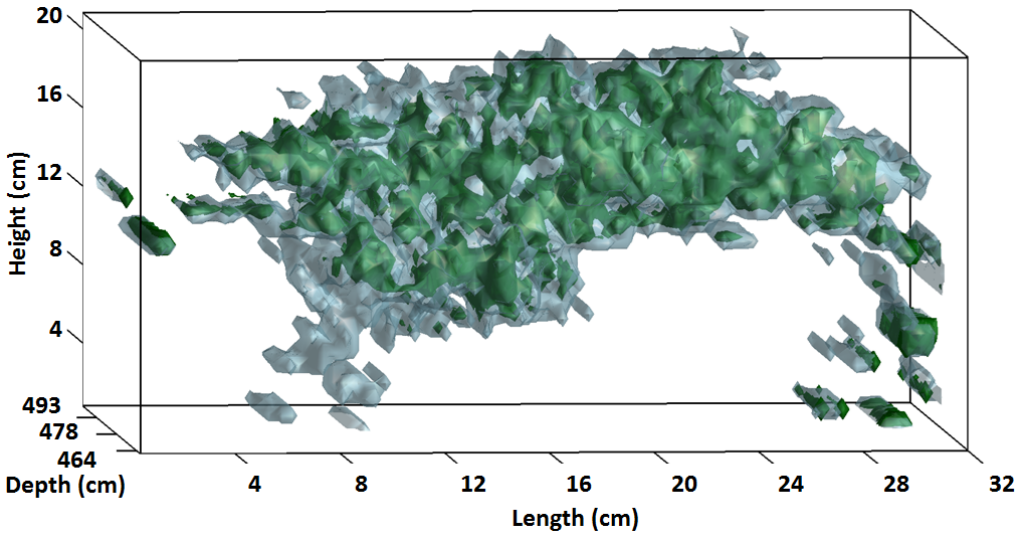

(a) *The created 3D-model of the scanned branch.*

(b) *The scanned branch of a Thuja.*

Figure 5.16: *Original branch and constructed model. The dark colour in (a) corresponds to the fluorescent (Chlorophyll) channel and the light colour to the elastic channel. Images created by Guangyu Zhao.*

6 Discussion & conclusions

6.1 Instrumental setup & characteristics

The LIDAR system was built with a very low budget compared to similar setups, partly to show the ability to construct an advanced and useful LIDAR with low cost. However, the restrictions of the setup due to the low-cost parts also put limits to what measurements could be performed in this thesis work. The target has mainly been zooplankton and due to their high transparency it has been impossible to detect both auto-fluorescence and limb oscillations, even if the elastic signal has been very strong. An increase in laser power could increase the strength of the inelastic scattering processes and allow for a better detection of the fluorescent signals, although proper focusing would probably have much greater impact on the detected signal strength.

The range resolution calibration showed that, in order to accurately resolve two organisms in one exposure, they need to be separated by approximately 10 cm in the far end of the tank. This is not in accordance with the raytracing modelling made by Ljungholm et. al. [1] and the reason is probably misalignment and defocusing. The present resolution might be too coarse for studies of the interaction between a small number of individuals as in the experiments performed in this study, but would be more than sufficient when mapping a larger number of individuals in large scale experiments as in the studies performed by Lemon et. al. [13]. To improve the range resolution, the focus problems would have to be solved. Moreover, the size of the detector system (i.e slit length, following optics and sensor) together with the separation between the detector system and the laser determines the close range. If the size of the detector system would be larger, the separation distance larger and the angles Θ and ϕ (shown in figure 2.9) changed accordingly, a better range resolution would be obtained at the cost of a larger system (cf. equation 8.

The range resolution is not only dependent on the separation of the backscattering objects but also on their size ratio and refractive index. A large opaque object will shadow the beam and reduce the intensity exposed to the following object, causing its backscattered signal to be weaker than the first objects. Two identical objects exposed to the beam simultaneously at different distances might therefore yield different responses. It would be very hard to compensate for these differences but by studying eventual extinction in the Raman channel after the object, one could be able to quantify the extinction and compensate for the weaker signal. Extinction can be measured in the elastic or Raman signals in some of the recorded events but the results are too inconclusive for any quantitative analysis.

Additionally, the laser beam size affects the range resolution. Since the Scheimpflug condition assumes an infinitely narrow laser beam (i.e. object plane), the wider the beam in the field of view plane, the larger the range span that corresponds to the same angle will be detected as the same range. This ultimately makes it harder to resolve organisms close together, and also to determine the actual range of the event. During the experiments performed in this study, only a few exposures during the aquatic measurements have contained several individuals in the beam. When comparing figure 3.10 with 3.12 it is clear that the current limitation is physical and not in the data handling (although, in this case, the limitation is due to defocusing). The ability to detect multiple objects in the beam might be more important during 3D-mapping experiments where the beam, for example, could penetrate a sparse foliage with multiple back scattering layers.

If the signal strength is increased, the binning of wavelength pixels can be reduced or removed. In the experiments performed in this study, 8 pixels were binned, which allows for a higher frame rate. This has also been done because of the need for a strong signal. With current optics, the system itself does not have good enough resolution to benefit from all wavelength pixels and in the experiments conducted there has been no need for higher wavelength resolution.

There seem to be a few focusing problems with the setup. When focusing the collecting lens at the slit, a half moon shaped pattern appear, as shown in figure 3.13. This could be a well-known problem with PGP setups when the light source is off axis and this problem is discussed by Aikio [48]. It has been noted that the actual configuration does not agree with the results from the ray tracing. It is not clear whether or not this is the cause for the focusing issues but this should be investigated before larger studies are performed with the setup. Since the detector is assembled using a mixture of prefabricated and hand made parts, it is rather complicated to disassemble and assemble and it is likely that some new parts might need to be constructed if the physical setup should match the model used in ray tracing.

The control programs developed in LabView are working very well. Initially there were some problems with the data recording but these issues have been solved and the control system now runs smoothly. It allows the user to run the program in continuous, modulation or periodic mode and displays the information in a clear way. A task that yet remains is to allow for wavelength and range calibration in the LabView program. At the moment, all information, spectral and range, is given in pixels. It would probably be easy to display the signals as functions of wavelength and distance instead. Another desired feature is the ability to store additional meta data in the binary files. It would be very practical if information about the custom parameters could be saved along with the detector resolution and the time stamp in the binary files. The physical control systems were also greatly improved by the custom built control box which was necessary for safety reasons.

6.2 Aquatic experiments

The initial dispersal experiment clearly showed that the *Daphnia* were attracted to the laser light. This could pose problems because of the need of a non-intrusive method when monitoring zooplankton. However, with a short duty cycle and a long pause time as was implemented in the subsequent experiments, and the fact that the final aim is to monitor in the field where the LIDAR will move rapidly across the probe area, this is not expected to be of great concern.

What differentiates this zooplankton monitoring technique with others is the ability to simultaneously detect temporal, spectral and range information. This could potentially enable monitoring of taxonomy, concentration and highly resolved dispersal dynamics, all at the same time. To be able to distinguish between e.g. different zooplankton species, the wavelength spectrum has to be unique for that species, and the auto-fluorescence has to be strong enough for detection. No auto-fluorescence signal could be obtained with the setup used, although the possibility to detect the auto-fluorescence from some aquatic animals has been proven by Shimomura [49]. Many of the components involved could be upgraded, but most importantly proper focus has to be achieved in order to detect both zooplankton auto-fluorescence and limb oscillations. Since a *Daphnia* is imaged on ca 20 range pixels instead of the expected 1-5 pixels, the fluorescence signal could be increased by approximately 100 times if the system was focusing properly (since it is defocused in two dimensions). Higher laser power could also improve the signal strength.

Due to the high transparency, small size and limb shape of zooplankton, the detection system has to be very sensitive to measure their limb oscillations. Due to the integrated filter which removes 99% of the elastic signal, the signal strength is low for very short exposure times and the system is not optimised for experiments that require a strong signal and high temporal resolution. The filter was integrated in the PGP to avoid misalignment, but an obvious upgrade of the system would be to install the filter externally to facilitate its removal. This was not done since realignment of the system would take a long time. The instrumental improvements suggested for detecting auto-fluorescence also applies for limb oscillations detection.

Because of the large volume of the tank, the relatively small probe volume defined by the laser beam size and the small size of *Daphnia* and *Chaoborus*, a large animal population was needed in order to obtain a decent amount of events. Even so, the event count per time unit was low when compared to LIDAR monitoring of airborne organism [43]. All the dispersal experiments proved to be unexpectedly hard to perform and deduce information from, especially those containing *Daphnia* and *Chaoborus*, mainly because of the lack of data generated. During the most successful experiment, 3846 events were obtained in 21 hours, resulting in a mean of 183 events / hour. However, only 52 of these events contained sufficient spectral information for an accurate species classification. The original purpose with the experiment of *Daphnia* and *Chaoborus* was to investigate and quantify the interaction strength between the two species, but due to the small amount of data this could not be done. Remarkably few events of *Chaoborus* were recorded, probably because they do not move as much as *Daphnia*.

The marker pen dying was a fast and cheap method to accurately differentiate between successfully dyed individuals of the different species, but it is clear that many of the *Daphnia* events recorded were without any dye fluorescence signal. Not even a trace of the dye fluorescence is apparent in many of these events, and possible explanations are that these *Daphnia* were either not coloured properly, the rinsing removed the dye, or the *Daphnia* were too small to contain enough dye for detection. A visual inspection of the dyed *Daphnia* indicated that most *Daphnia* indeed seemed to be successfully dyed, which indicates that the most probable explanation for the lack of detected fluorescence signals is that the smaller *Daphnia* did not contain enough fluorescent dye for detection. Another problem worth mentioning was that many of the different coloured marker pens that were evaluated as dye seemed to consist of the same fluorescent substances in different mixes. This was manifested when seemingly different colours had overlapping fluorescence spectra. It can be seen in figure 5.2 where the three different colours seems to consist of two peaks at 600 and 540 nm.

The periodic structure in figure 5.12 and 5.14 has been investigated but no conclusion could be drawn. Optical reasons such as interference from the grating and free spectral range in optical components acting as Fabry–Pérot interferometers have been investigated. The wavelength separation of 23 nm corresponds to a thickness of 3 µm for a Fabry-Pérot interferometer which is roughly one order of magnitude below the thinnest component. The interference from the transmission grating has not been simulated but since it would cause an increasing separation with wavelength, it is deemed unlikely. Another explanation which is discarded since it would cause increasing separations between the peaks is the transmission curve of the long pass filter. Further work is needed to investigate properties of the detector, uneven heating, and currents could cause errors in the camera, even if all optical components were flawless. Since the structure appear even for untreated data, as in figure 5.14 where the only data treatment performed in Matlab is the median and sum over all images, numerical errors also seems to be unlikely.

The experiment results were largely dependent on the water quality in the tank. Water directly from the tap was used at first, which significantly attenuated the beam. The water was changed to non aerated water, with a dramatic increase in the signal strength and reduction of the scattering from water. Turbidity in the water could pose problems if used in the field and will dramatically reduce the penetration depth. A solution to this could be to submerge the system in the water to the desired depth and probe both in all directions, and/or use a laser with higher power. Attenuation can also be compensated for by using longer exposure times. The dynamical intensity span will decrease, since the closer volume would saturate the intensity in turbid water.

A factor worth to consider when measuring in the field is light sources in the probe volume, such as bioluminescent organisms. These light sources would however be easy to detect since they also would appear in the "dark" exposures when the laser is turned of. With sufficient signal strength, their luminance spectra could be recorded and used for species classification.

6.3 Plant Scanning

This experiment showed the flexibility of the instrument and that it is not restricted to aquatic use. However, the system could certainly be better optimised for use in air. One problem is that the elastic signal is very strong compared to the fluorescent light. This problem could be solved by inserting a stronger, or an additional long pass filter into the detector. With the current detector setup, there is however no easy way to perform such changes if one wants to avoid realignment. The largest limiting factor with the current setup was the uneven movement of the plant. Given a smoother way to move the plant, or alternatively move the laser, the resolution could be greatly improved, ultimately only limited in range by equation 8.

Laser profiling of vegetation structure is however, as shown by this simple experiment, easily done even with the current setup and the technique is, to the authors' knowledge, significantly more advanced than commercially available systems. Future applications could consist of mounting a larger version of the system on an airplane mapping forests, or a lighter system on a remote controlled drone. This would allow for hyperspectral 3D-mapping of large areas where one could identify the vegetation distribution and eventually identify different species with spectral analysis. Similarly, the aquatic bottom vegetation could be mapped from a boat or by submerging the system. This would require further development of the data processing. The current method requires image selection and arrangement by hand which is time consuming and impossible for large scale measurements. However, given an accurate way of controlling the position of the laser beam, the process could easily be automated.

A problem specific for the Scheimpflug setup when performing experiments on macroscopic objects is that protruding objects might obscure the field of view. This problem sometimes appeared during preparatory experiments performed with the setup before the complete 3D-mapping was done. The experiments in this study were however performed at a distance of roughly 5 m. A large scale application of the technique would probably operate at much larger distances which would reduce the problem since the field of view would be more narrow. On the other hand would a more narrow field of view lead to reduced range resolution.

7 Outlook

The results of this thesis shows a promising future for hyperspectral LIDAR monitoring of plankton, as well as other applications. Because of the small size and weight of the system, it may be used in many different applications, such as vertical mapping of the water column from a boat, deep water monitoring with the use of a submersible vehicle, or mapping of terrestrial vegetation from a drone. Even though the sensitivity and spatial and temporal resolutions are increased compared to earlier described systems, both the range and wavelength resolution can be improved greatly, since most components can be upgraded. Scaled up versions could be used to monitor atmospheric major constituents using the Raman scattering as calibration, or to measure on fluorescent constituents such as pollen or dangerous agents. Laser safety, is of concern, especially in air where attenuation is lower, although the laser wavelength could be chosen below the critical eye safety limit of 400 nm. A study has shown that the eyes of some marine mammals are less sensitive than a human eye, which implies that laser safety limits for humans are sufficient [50]. However, further studies has to be made to ensure the safety of the method.

This thesis work has shown the possibility to employ a non-intrusive monitoring method of zooplankton based on a hyperspectral Scheimpflug LIDAR. It has been demonstrated that the position as well as type of organism can be determined, and time-resolved distribution can easily be achieved. The potential for detecting auto-fluorescence, as well as limb detections, is high with further development of the system. Either as a stand-alone system or a complement to other monitoring systems, it has a great potential for use in environmental monitoring.

References

[1] Mikael Ljungholm. Inelastic lidar for monitoring aquatic fauna. *Unpublished*, 2016.

[2] Iain M Suthers and David Rissik. *Plankton: A guide to their ecology and monitoring for water quality*. Csiro Publishing, 2009.

[3] HW Ducklow, CA Carlson, NR Bates, AH Knap, AF Michaels, T Jickells, PJ Le B Williams, and IN McCave. Dissolved organic carbon as a component of the biological pump in the north atlantic ocean [and discussion]. *Philosophical Transactions of the Royal Society of London B: Biological Sciences*, 348(1324):161–167, 1995.

[4] Daphnia magna. `http://www.oceannetworks.ca/ocean-acoustics`. Accessed: 2016-04-18.

[5] Copepod calanus. `http://www.warrenphotographic.co.uk/photography/bigs/16369-Marine-planktonic-copepod.jpg`. Accessed: 2016-04-22.

[6] Grégory Beaugrand. Monitoring pelagic ecosystems using plankton indicators. *ICES Journal of Marine Science: Journal du Conseil*, 62(3):333–338, 2005.

[7] James H Churnside and Richard E Thorne. Comparison of airborne lidar measurements with 420 khz echo-sounder measurements of zooplankton. *Applied optics*, 44(26):5504–5511, 2005.

[8] P Koeller, C Fuentes-Yaco, T Platt, S Sathyendranath, A Richards, P Ouellet, D Orr, U Skúladóttir, Kai Wieland, L Savard, et al. Basin-scale coherence in phenology of shrimps and phytoplankton in the north atlantic ocean. *science*, 324(5928):791–793, 2009.

[9] John Raven, Ken Caldeira, Harry Elderfield, Ove Hoegh-Guldberg, Peter Liss, Ulf Riebesell, John Shepherd, Carol Turley, and Andrew Watson. *Ocean acidification due to increasing atmospheric carbon dioxide*. The Royal Society, 2005.

[10] Brian Petrie, Kenneth T Frank, Nancy L Shackell, and William C Leggett. Structure and stability in exploited marine fish communities: quantifying critical transitions. *Fisheries Oceanography*, 18(2):83–101, 2009.

[11] Joseph A Shaw, James H Churnside, James J Wilson, Nicole E Lerner, Rianon R Tiensvold, Patricia E Bigelow, and Todd M Koel. Airborne lidar mapping of invasive lake trout in yellowstone lake. In *Proceedings of the 24th International Laser Radar Conference*, volume 11, pages 905–908, 2008.

[12] James H Churnside, David A Demer, and Behzad Mahmoudi. A comparison of lidar and echosounder measurements of fish schools in the gulf of mexico. *ICES Journal of Marine Science: Journal du Conseil*, 60(1):147–154, 2003.

[13] DD Lemon, RA Chave, MR Clarke, RK Dewey, and P Macoun. Inverted echo sounder on a cabled observatory. In *OCEANS 2007*, pages 1–7. IEEE, 2007.

[14] Ocean acoustics. `http://www.oceannetworks.ca/ocean-acoustics`. Accessed: 2016-04-18.

[15] Joseph D Warren. Estimating gulf of marine zooplankton distributions using multiple frequency acoustic, video and environmental data. Technical report, DTIC Document, 2001.

[16] Peter H Wiebe, Timothy K Stanton, Charles H Greene, Mark C Benfield, Heidi M Sosik, Thomas C Austin, Joseph D Warren, and Terry Hammar. Biomaper-ii: an integrated instrument platform for coupled biological and physical measurements in coastal and oceanic regimes. *Oceanic Engineering, IEEE Journal of*, 27(3):700–716, 2002.

[17] Sample data of the biomaper ii. `http://www.whoi.edu/cms/images/instruments/2006/4/sampledata_23597.jpg`. Accessed: 2016-05-18.

[18] J Katz, PL Donaghay, J Zhang, S King, and K Russell. Submersible holocamera for detection of particle characteristics and motions in the ocean. *Deep Sea Research Part I: Oceanographic Research Papers*, 46(8):1455–1481, 1999.

[19] CS Davis, SM Gallager, MS Berman, LR Haury, and JR Strickler. The video plankton recorder (vpr): design and initial results. *Arch. Hydrobiol. Beih*, 36:67–81, 1992.

[20] Dieter Ebert. *Ecology, epidemiology, and evolution of parasitism in Daphnia*. National Center for Biotechnology Information (US), 2005.

[21] N.N. Smirnov. *Physiology of the Cladocera*. Elsevier Science, 2013.

[22] Drawing of daphnia. `http://pulse.pharmacy.arizona.edu/9th_grade/culture_cycles/science/handouts/daphnia_named.jpg`. Accessed: 2016-05-18.

[23] Carl N Von Ende. Phenology of four chaoborus species. *Environmental Entomology*, 11(1):9–16, 1982.

[24] Michael C Swift and Alice Y Fedorenko. Some aspects of prey capture by chaoborus larvae. *Limnology and Oceanography*, 20(3):418–425, 1975.

[25] Chaoborus. `http://www.microscopy-uk.org.uk/mag/imagsmall/chaoborus2.jpg`. Accessed: 2016-04-18.

[26] Sune Svanberg. *Multi-Spectral Imaging from astronomy to microscopy - from radiowaves to gammarays*. Department of Physics, Lund University, 2nd edition, 2015.

[27] Bahaa EA Saleh, Malvin Carl Teich, and Bahaa E Saleh. *Fundamentals of photonics*. Wiley New York, 2nd edition, 2007.

[28] Sune Svanberg. *Atomic and molecular spectroscopy: basic aspects and practical applications; with 14 tables*. Springer Science & Business Media, 2004.

[29] Sune Svanberg. *Fluorescence Spectroscopy and Imaging of Lidar Targets*, pages 433–467. Optical Science and Engineering. CRC Press, Jun 2005. 0.

[30] P. S. Andersson, E. Kjellén, S. Montán, K. Svanberg, and S. Svanberg. Autofluorescence of various rodent tissues and human skin tumour samples. *Lasers in Medical Science*, 2(1):41–49, 1987.

[31] Fluorescence. `http://icecube.berkeley.edu/~bramall/work/astrobiology/fluorescence.htm`. Accessed: 2016-05-04.

[32] Water structure and science. `http://www1.lsbu.ac.uk/water/water_vibrational_spectrum.html`. Accessed: 2016-01-25.

[33] Seos-project. `http://www.seos-project.eu/modules/laser-rs/laser-rs-c07-s03-p05.html`. Accessed: 2016-01-25.

[34] Craig F Bohren and Donald R Huffman. *Absorption and scattering of light by small particles*. John Wiley & Sons, 2008.

[35] Siamak Khorram, Stacy A.C. Nelson, Frank H. Koch, and Cynthia F. van der Wiele. *Remote Sensing*. SpringerBriefs in Space Development. Boston, MA : Springer US, 2012.

[36] Harold M Merklinger. Scheimpflug's patent. *Photo Techniques*, 17(6):56, 1996.

[37] Liang Mei and Mikkel Brydegaard. Atmospheric aerosol monitoring by an elastic scheimpflug lidar system. *Optics Express*, 23(24):A1613 – A1628, 2015.

[38] Liang Mei and Mikkel Brydegaard. Continuous-wave differential absorption lidar. *Laser & Photonics Reviews*, 9(6):629–636, 2015.

[39] Ronald AJ Litjens, Terence I Quickenden, and Colin G Freeman. Visible and near-ultraviolet absorption spectrum of liquid water. *Applied Optics*, 38(7):1216–1223, 1999.

[40] Robin M. Pope and Edward S. Fry. Absorption spectrum (380–700 nm) of pure water. ii. integrating cavity measurements. *Appl. Opt.*, 36(33):8710–8723, Nov 1997.

[41] Water absorption spectrum. `http://omlc.org/spectra/water/abs/index.html`. Accessed: 2016-05-16.

[42] W. Scott Pegau, Deric Gray, and J. Ronald V. Zaneveld. Absorption and attenuation of visible and near-infrared light in water: dependence on temperature and salinity. *Appl. Opt.*, 36(24):6035–6046, Aug 1997.

[43] E. Malmqvist, S. Jansson, S. Török, and M. Brydegaard. Effective parameterization of laser radar observations of atmospheric fauna. *IEEE Journal of Selected Topics in Quantum Electronics*, 22(3):1–8, May 2016.

[44] John Shlens. A tutorial on principal component analysis. `https://www.cs.princeton.edu/picasso/mats/PCA-Tutorial-Intuition_jp.pdf`. Accessed: 2016-04-21.

[45] Alan Kaylor Cline and Inderjit S. Dhillon. Computation of the singular value decomposition. `http://www.cs.utexas.edu/users/inderjit/public_papers/HLA_SVD.pdf`. Accessed: 2016-04-21.

[46] Singular value decomposition (svd) tutorial. `http://web.mit.edu/be.400/www/SVD/Singular_Value_Decomposition.htm`. Accessed: 2016-04-21.

[47] Thomas C O'Keefe, Matthew C Brewer, and Stanley I Dodson. Swimming behavior of daphnia: its role in determining predation risk. *Journal of Plankton Research*, 20(5):973–984, 1998.

[48] M Aikio. *Hyperspectral prism-grating-prism imaging spectrograph*. PhD thesis, PhD thesis, 2001.

[49] Osamu Shimomura. Discovery of green fluorescent protein (gfp)(nobel lecture). *Angewandte Chemie International Edition*, 48(31):5590–5602, 2009.

[50] Heather M Zorn, James H Churnside, and Charles W Oliver. Laser safety thresholds for cetaceans and pinnipeds. *Marine mammal science*, 16(1):186–200, 2000.